Annu. Rev. Nucl. Part. Sci. 2006. 56:293–326
doi: 10.1146/annurev.nucl.56.080805.140513

First published online as a Review in Advance on July 5, 2006

SEARCHES FOR ASTROPHYSICAL AND COSMOLOGICAL AXIONS*

Stephen J. Asztalos,[1] Leslie J Rosenberg,[1] Karl van Bibber,[1] Pierre Sikivie,[2,3] and Konstantin Zioutas[4]

[1]*Lawrence Livermore National Laboratory, Livermore, California 94550; email: asztalos1@llnl.gov, ljrosenberg@llnl.gov, vanbibber1@llnl.gov*
[2]*Institute for Advanced Study, Princeton, New Jersey 08540*
[3]*University of Florida, Gainesville, Florida 32611; email: sikivie@phys.ufl.edu*
[4]*University of Patras, GR 26500 Patras, Greece and CERN, Geneva, Switzerland; email: zioutas@cern.ch*

Key Words dark matter, RF cavity, solar telescope

■ **Abstract** The axion, a favored dark matter candidate, is expected to have a very small mass and extraordinarily weak couplings. Although it has eluded discovery or exclusion for three decades, it remains the most compelling solution to the strong-CP problem. Axions may be detected by their resonant conversion to RF photons in a microwave cavity permeated by a magnetic field. Experiments have already set significant limits on the axion's mass and photon coupling; progress in photon detection schemes at or below the standard quantum limit will soon enable definitive searches. Similarly, axions produced in the solar burning core may be detectable by their conversion to X rays in a magnetic helioscope. Significant improvements in both mass range and sensitivity of the axion helioscope will likewise be forthcoming in the next few years.

CONTENTS

1. DEDICATION

This review is dedicated to the memory of Joe Rogers, whose Ph.D. thesis was the first dissertation ever on a microwave axion search (1). Joe was a highly talented experimental physicist and, most importantly, a wonderful person and friend (Figure 1). At the time of his death, he was an Associate Professor at Cornell, where his research was devoted to accelerator physics.

Figure 1 Joseph Thomas Rodgers (1957–2004).

2. INTRODUCTION

The axion is replete with paradox. Arising from the unexpected conservation of CP symmetry in the strong interaction, the axion would be the most weakly interacting of all particles, neglecting the gravitational force. A plausible candidate for constituting most of the matter in the universe, it is possibly the lightest of all elementary particles with nonzero mass. If ever discovered, it will almost certainly be from cosmological or astrophysical sources and may never be detected in purely laboratory experiments.

Notwithstanding its elusive nature, physicists are making excellent progress in both sectors, i.e., searches for axions constituting our galactic halo dark matter and for axions emitted from the solar burning core (and possibly from other active sources). Here, we review this progress and prospects for definitive answers—but a brief history is first in order.

In 1977, Roberto Peccei and Helen Quinn, both then at SLAC, discovered a simple and elegant solution to the strong-CP problem (2), in particular, the puzzling absence of a neutron electric dipole moment, the present limit of which is $<0.63 \times 10^{-25}$ e $\times$ cm (3). Soon after, Steven Weinberg and Frank Wilczek realized independently that the Peccei-Quinn (PQ) solution implied the existence of a light pseudoscalar, termed the axion (4). As the symmetry-breaking scale within the PQ mechanism was posited (for no particular reason) to be the electroweak scale $f_A \approx f_{EW}$, the axion's mass was expected to be on the order of hundreds of keV, and its couplings sufficiently strong to be seen in accelerator and reactor experiments. After a few years, however, the experimental situation clearly disfavored these standard axions. Subsequently, theorists developed new models with arbitrarily large f_A, resulting in couplings so extraordinarily weak (m_A, $g_{Aii} \propto f_A^{-1}$) as to render the axion effectively invisible. Tantalizingly, however, driving up the symmetry-breaking scale also drives up the cosmological abundance ($\Omega_A \propto f_A^{7/6}$), making a sufficiently light axion an excellent dark matter candidate (5). Figure 2

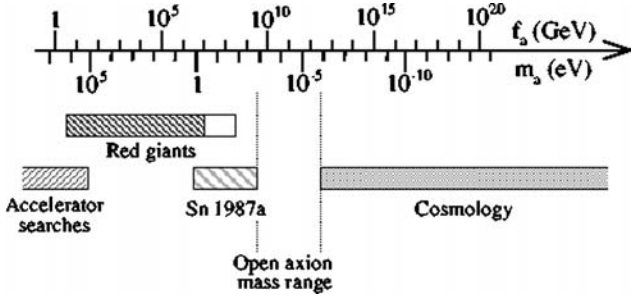

Figure 2 The allowed axion mass range, bounded from below by the requirement that axions should not overclose the universe and from above by accelerator searches and stellar evolution.

shows the current bounds on the axion mass. The lower end of the allowed mass region $10^{-6} < m_A < 10^{-3}$ eV is derived from the requirement that axions should not overclose the universe. The upper mass limit is where axions would begin to modify observed stellar evolution. In 1983 Sikivie (6) solved the conundrum that the dominant form of matter in the universe might well be undetectable. The key insight was to search for axions through their two-photon coupling and, more precisely, through their Primakoff interaction, i.e., the conversion of a pseudoscalar into a single real photon in an electromagnetic field. Specifically, the concept was to look for galactic halo axions by their resonant conversion to a monochromatic microwave signal in a high-Q cavity permeated by a strong magnetic field. The proposal was well grounded in the existing and projected state of the required technologies, i.e., superconducting magnets, microwave cavities, and ultra-low-noise RF detection. Cosmological axions finally seemed within reach. This paper also applied axion-photon conversion to look for relativistic axions emitted from the sun's burning core, the axion helioscope. Such axions might be detected if $g_{A\gamma\gamma}$ were sufficiently strong, yet well below the level at which the fluence of free-streaming axions would begin to disrupt the agreement between solar evolution models and observation. The Sikivie paper proved prescient insofar as both concepts provoked experimental campaigns, each now in their third generation of increasing scale and sophistication.

The reader is directed to older but still largely relevant reviews of axion theory (7, 8), astrophysical and cosmological constraints (9), and, specifically, stellar evolution limits (stars as laboratories) (10, 11). More recent reviews have appeared on experimental searches for the invisible axion (12) and, more specifically, on the microwave cavity technique for dark matter axions (13).

3. THEORY OF THE AXION

Axion-like excitations are a feature of many particle theories. Below we review axion properties in generic axion models and in models with large extra dimensions.

3.1. Generic Axion Models

The Standard Model of elementary particles (14) has been an extraordinary breakthrough in our description of the physical world. It agrees with experiment and observation disconcertingly well and provides the foundation for all further progress in our field. However, it also presents us with a puzzle.

The action density of the Standard Model includes, in general, a term

$$\mathcal{L}_{\text{stand mod}} = \cdots + \frac{\theta g^2}{32\pi^2} G^a_{\mu\nu} \tilde{G}^{a\mu\nu}, \qquad 1.$$

where $G^a_{\mu\nu}$ are the QCD field strengths, g is the QCD coupling constant, and θ is a parameter. The dots represent the other terms in the action density, i.e., the

terms that lead to the numerous successes of the Standard Model. Equation 1 displays the one term that is not a success. Using the statement of the chiral anomaly (15), one can prove three statements about that term: first, that QCD physics depends on the value of the parameter θ because in the absence of such dependence, QCD would have a $U_A(1)$ symmetry in the chiral limit, and we know QCD has no such $U_A(1)$ symmetry (16); second, that θ is periodic, that is, physics at θ is indistinguishable from physics at $\theta + 2\pi$; and third, that the combination of Standard Model parameters $\bar{\theta} \equiv \theta - \arg\det m_q$, where m_q is the quark mass matrix, is independent of quark field redefinitions. Physics therefore depends on θ solely through $\bar{\theta}$. Because the term shown in Equation 1 is a four-divergence, the $\bar{\theta}$ dependence of the Standard Model is entirely due to nonperturbative effects. The relevant nonperturbative effects (17) are tunneling events between QCD vacua described by instanton solutions (18) of the Yang-Mills field equations in Euclidean space.

Because physics depends on $\bar{\theta}$, the value of $\bar{\theta}$ is determined by experiment. The term shown in Equation 1 violates P and CP. This source of P and CP violation is incompatible with the experimental upper bound on the neutron electric dipole moment (19) unless $|\bar{\theta}| < 10^{-10}$. The aforementioned puzzle is why the value of $\bar{\theta}$ is so small. It is usually referred to as the strong-CP problem. If there were only strong interactions, a zero value of $\bar{\theta}$ could be simply a consequence of P and CP conservation. That would not be much of a puzzle. However, there are also weak interactions and they, and therefore the Standard Model as a whole, violate P and CP. Thus, these symmetries cannot be invoked to set $\bar{\theta} = 0$. More pointedly, P and CP violation are introduced in the Standard Model by allowing the elements of the quark mass matrix m_q to be arbitrary complex numbers (20). In that case, one expects $\arg\det m_q$, and hence $\bar{\theta}$, to be a random angle.

The puzzle is removed if instead the action density is

$$\mathcal{L}_{\text{stand mod + axion}} = \cdots + \frac{1}{2}\partial_\mu A \partial^\mu A + \frac{g^2}{32\pi^2}\frac{A(x)}{f_A} G^a_{\mu\nu}\tilde{G}^{a\mu\nu}, \qquad 2.$$

where $A(x)$ is a new scalar field and the dots represent the other terms of the Standard Model. f_A is a constant with dimension of energy. The $AG \times \tilde{G}$ interaction in Equation 2 is not renormalizable. However, there is a recipe for constructing renormalizable theories whose low-energy effective action density is of the form of Equation 2. The recipe is as follows: Construct the theory in such a way that it has a $U(1)$ symmetry, which is a global symmetry of the classical action density, is broken by the color anomaly, and is spontaneously broken. Such a symmetry is termed PQ symmetry (2). Weinberg and Wilczek (4) pointed out that a theory with a $U_{\text{PQ}}(1)$ symmetry has a light pseudoscalar particle, known as the axion. The axion field is $A(x)$. f_A is of order the expectation value that breaks $U_{\text{PQ}}(1)$ and is termed the axion decay constant.

In the theory defined by Equation 2, $\bar{\theta} = \frac{A(x)}{f_A} - \arg\det m_q$ depends on the expectation value of $A(x)$. That expectation value minimizes the effective potential. The strong-CP problem is then solved because the minimum of the QCD effective

potential $V(\bar{\theta})$ occurs at $\bar{\theta} = 0$ (21). The weak interactions induce a small value for $\bar{\theta}$, of order 10^{-17} (22), but this is consistent with experiment.

The notion of PQ symmetry may seem contrived. Why should there be a $U(1)$ symmetry that is broken at the quantum level but is exact at the classical level? Keep in mind, however, that the reasons for PQ symmetry may be deeper than we know at present. String theory contains many examples of symmetries that are exact classically, but are broken by anomalies, including PQ symmetry. Also, within field theory are examples of theories with automatic PQ symmetry, i.e., in which PQ symmetry is just a consequence of the particle content of the theory, without adjusting parameters to special values.

The properties of the axion can be derived using the methods of current algebra (23). The axion mass is given in terms of f_A by

$$m_A \simeq 6 \text{ eV} \frac{10^6 \text{GeV}}{f_A}. \quad 3.$$

The first axion models had f_A of order the weak-interaction scale and it was thought that this was an unavoidable property of axion models. However, it was soon pointed out (24, 25) that the value of f_A is in fact arbitrary, that it is possible to construct axion models with any value of f_A from the QCD scale to the Planck scale. The value of f_A may be related to, and of order, the scale of a new strong interaction whose condensates break $U_{\text{PQ}}(1)$ spontaneously (26).

All the axion couplings are inversely proportional to f_A. For example, the axion coupling to two photons is

$$\mathcal{L}_{A\gamma\gamma} = -g_\gamma \frac{\alpha}{\pi} \frac{A(x)}{f_A} \vec{E} \cdot \vec{B}. \quad 4.$$

Here, $\vec{E}$ and $\vec{B}$ are the electric and magnetic fields, α is the fine-structure constant, and g_γ is a model-dependent coefficient of order unity. $g_\gamma = 0.36$ in the DFSZ (Dine, Fischler, Srednicki & Zhitnitsky) model (24), whereas $g_\gamma = -0.97$ in the KSVZ (Kim, Shifman, Vainshtein & Zakharov) model (25). The coupling of the axion to a spin-1/2 fermion f has the form

$$\mathcal{L}_{A\bar{f}f} = i g_f \frac{m_f}{f_A} A \bar{f} \gamma_5 f, \quad 5.$$

where g_f is a model-dependent coefficient of order one. In the KSVZ model, the coupling to electrons is zero at tree level. Models with this property are termed hadronic.

3.2. Large Extra Dimensions

In recent years, theories with extra spatial dimensions were invented to address the hierarchy problem of particle physics, i.e., the large separation between the electroweak scale and the Planck scale. In the model with large extra dimensions

of Arkani-Hamed, Dimopoulos & Dvali (ADD) (27, 28) the n extra dimensions are compactified with a relatively large radius R and the geometry of space is flat. The fundamental scale of gravity is no longer the Planck scale $M_{\rm Pl}$, but rather the corresponding higher-dimensional scale M_D that can be close to TeV energies. The hierarchy is generated by the large volume of the extra dimensional space [$M_{\rm Pl} \approx M_D(RM_D)^{n/2}$]. In the ADD model, extra dimensions are felt only by gravity (as well as other fields transforming as singlets under the Standard Model gauge group). The Standard Model fields are confined to a $(3 + 1)$-dimensional subspace (brane) of a higher-dimensional space (bulk). The absence of any observed deviation from ordinary Newtonian gravity in Cavendish-type laboratory experiments, for the case $n = 2$, implies that the largest compactification radius is smaller than approximately 0.15 mm. Astrophysical limits, which depend, however, on techniques and assumptions, are much more stringent and can be as low as a few nanometers for the case $n = 2$.

In addition to gravity, axions too could propagate in $\delta \leq n$ extra dimensions. Axions are singlets under the Standard Model gauge group, so they are allowed to propagate in the bulk. However, according to astrophysical and cosmological considerations, the PQ scale $f_{\rm PQ}$ should be much greater than the fundamental scale M_D. To avoid a new hierarchy problem, axions should propagate in the extra dimensions. Then the higher-dimensional scale $\bar{f}_{\rm PQ}$ can be lowered by the same mechanism, as in the case of gravity.

The higher-dimensional axion field is Fourier expanded in the δ-additional spatial dimensions into a complete set of modes—the so-called Kaluza-Klein (KK) tower of states. KK excitations have an almost equidistant mass spacing of order $1/R$. The lowest KK state may be identified with the ordinary PQ axion and specifies the coupling strength of each KK state to matter. A source of axions, such as the sun, will emit all KK states with a mass up to the kinematic limit, i.e., some keV. Another interesting feature arising from the higher-dimensional axionic theories is that the axion mass may decouple from the PQ energy scale (in four-dimensional theories, $m_{\rm PQ} \sim 1/f_{\rm PQ}$) (29). In such cases, the axion mass is determined by the compactification radius ($m_A \simeq 1/2R$) (30).

4. COSMOLOGICAL AXIONS

This section explains why an axion with mass on the order of 10^{-5} eV is a cold dark matter (CDM) candidate and gives the characteristic properties of CDM axions.

4.1. Axion Cosmology

It may seem surprising that a particle of mass 10^{-5} eV is a CDM candidate because, to qualify as such, CDM particles must be nonrelativistic well before the epoch of galaxy formation. Indeed, axions of mass 10^{-5} eV and energy on the order of the cosmic microwave background radiation (CMBR) temperature today

($2.725\ \mathrm{K} = 2.348\ 10^{-4}$ eV) would be relativistic and unable to cluster into galactic halos. However, the point is that there are two populations of cosmic axions, which we term thermal and nonthermal. The first population is produced by thermal processes in the early universe (such as $g + g \rightarrow g + A$ and $q + g \rightarrow q + A$ scattering, where q is a quark and g is a gluon) and have temperature on the order of 1 K today, similar to CMBR photons and cosmic neutrinos.

The nonthermal axions have a different origin and are vastly colder than the thermal axions. They are produced during the QCD phase transition because the background axion field is initially displaced from the minimum of its effective potential. Below we see that their present energy density is a decreasing function of the axion mass and that the requirement that the nonthermal axions do not overclose the universe implies a lower limit on the axion mass on the order of 10^{-5} eV, with, however, large uncertainties.

To understand the appearance of the nonthermal axion population, we must consider the evolution of the universe from the very early time when the temperature was much larger than f_A and the $U_{\mathrm{PQ}}(1)$ symmetry was restored. A phase transition, usually known as the PQ phase transition, occurs at a temperature on the order of f_A, during which the $U_{\mathrm{PQ}}(1)$ symmetry is spontaneously broken. At these temperatures, the nonperturbative QCD effects that produce the effective potential $V(\bar{\theta})$ are negligible (31), the axion is massless, and all values of $\langle A(x) \rangle$ are equally likely. Axion strings appear as topological defects. One must distinguish between two scenarios depending on whether inflation occurs with reheat temperature lower (case 1) or higher (case 2) than the PQ transition temperature. In case 1, the axion field is homogenized by inflation and the axion strings are "blown" away.

When the temperature approaches the QCD scale, the potential $V(\bar{\theta})$ turns on and the axion acquires mass. There is a critical time, defined by $m_A(t_1)t_1 = 1$, when the axion field starts to oscillate in response to the turn-on of the axion mass. The corresponding temperature $T_1 \simeq 1$ GeV (5). The initial amplitude of this oscillation is how far from zero the axion field lies when the axion mass turns on. The axion-field oscillations do not dissipate into other forms of energy and hence contribute to the cosmological energy density today (5). This contribution is known as vacuum realignment. It is further described below. Note that the vacuum-realignment contribution may be suppressed accidentally in case 1 if the homogenized axion field happens to lie close to zero.

In case 2, the axion strings radiate axions (32, 33) from the time of the PQ transition until t_1, when the axion mass turns on. At t_1, each string becomes the boundary of N domain walls. If $N = 1$, the network of walls bounded by strings is unstable (34) and decays away. If $N > 1$, there is a domain-wall problem (35) because axion domain walls end up dominating the energy density, resulting in a universe very different from the one observed today. There is a way to avoid this problem by introducing an interaction that slightly lowers one of the N vacua with respect to the others. In that case, the lowest vacuum takes over after some time and the domain walls disappear. There is little room in parameter space for that to

happen, and we do not consider this possibility further here. A detailed discussion is given in Reference 36. Henceforth, we assume $N = 1$.

In case 2 there are three contributions to the axion cosmological energy density. One contribution (32, 33, 37–40) is from axions that were radiated by axion strings before t_1. A second contribution is from axions that were produced in the decay of walls bounded by strings after t_1 (36, 38, 41, 42). A third contribution is from vacuum realignment (5).

We indicate briefly how the vacuum-alignment contribution is evaluated. Before time t_1, the axion field did not oscillate even once. Soon after t_1, the axion mass is assumed to change sufficiently slowly so that the total number of axions in the oscillations of the axion field is an adiabatic invariant. The number density of axions at time t_1 is

$$n_A(t_1) \simeq \frac{1}{2} m_A(t_1)\ \langle A^2(t_1)\rangle \simeq \pi f_A^2 \frac{1}{t_1}. \qquad 6.$$

In Equation 6, we used the fact that the axion field $A(x)$ is approximately homogeneous on the horizon scale t_1. Wiggles in $A(x)$, which entered the horizon long before t_1, have been redshifted away (43). We also used the fact that the initial departure of $A(x)$ from the nearest minimum is on the order of f_A. The axions of Equation 6 are decoupled and nonrelativistic. Assuming that the ratio of the axion number density to the entropy density is constant from time t_1 until today, one finds (5, 36)

$$\Omega_A \simeq \frac{1}{2}\left(\frac{0.6 \times 10^{-5}\ \text{eV}}{m_A}\right)^{\frac{7}{6}} \left(\frac{0.7}{h}\right)^2 \qquad 7.$$

for the ratio of the axion energy density to the critical density for closing the universe. h is the present Hubble rate in units of 100 km s^{-1} Mpc^{-1}. The requirement that axions do not overclose the universe implies the constraint $m_A \geq 6 \times 10^{-6}$ eV.

The contribution from axion string decay has been debated over the years. The main issues are the energy spectrum of axions radiated by axion strings and the density of the axion string network in the early universe. In Reference 38 the contribution from string decay is estimated to be of the same order as that from vacuum realignment, whereas in References 39 and 40 it is estimated to be respectively 10 and 3 times larger, implying correspondingly more severe bounds on the axion mass. The contribution from wall decay was discussed in Reference 36. It is probably subdominant compared with the vacuum realignment and string decay contributions.

We emphasize that there are many sources of uncertainty in the cosmological axion energy density, aside from the uncertainty about the contribution from string decay. The axion energy density may be diluted by the entropy release from heavy particles that decouple before the QCD epoch but decay afterward (44), or by the entropy release associated with a first-order QCD phase transition. Alternatively, if the QCD phase transition is of first order (45), an abrupt change of the axion mass at the transition may increase Ω_A. If inflation occurs with reheat temperature less

than T_{PQ}, there may be an accidental suppression of Ω_A because the homogenized axion field happens to lie close to a CP-conserving minimum. Because the RHS of Equation 7 is multiplied in this case by a factor of order the square of the initial vacuum misalignment angle $\frac{A(t_1)}{f_A}$, which is randomly chosen between $-\pi$ and $+\pi$, the probability that Ω_A is suppressed by a factor x is on the order of $\sqrt{x}$. This rule cannot be extended to arbitrarily small x however because quantum mechanical fluctuations in the axion field during the epoch of inflation do not allow the suppression to be perfect (46). Recently, Kaplan & Zurek proposed a model (47) in which the axion decay constant f_A is time dependent, the value $f_A(t_1)$ during the QCD phase transition being much smaller than the value f_A today. This yields a suppression of the axion cosmological energy density by a factor of $(\frac{f_A(t_1)}{f_A})^2$, compared with the usual case [replace f_A by $f_A(t_1)$ in Equation 6)].

4.2. Axionic Dark Matter

Axions produced when their mass turns on during the QCD phase transition are CDM because they are nonrelativistic from the moment of their first appearance at 1 GeV temperature. Their velocity dispersion today is very small, on the order of 3×10^{-17} c $(\frac{10^{-5}\ \mathrm{eV}}{m_A})^{\frac{5}{6}}$ in case 2 and practically zero in case 1. Any form of CDM necessarily contributes to galactic halos by falling into the gravitational wells of galaxies. Hence, there is excellent motivation to look for axions as constituent particles of our galactic halo.

The small velocity dispersion of the CDM axions means that these particles lie, initially and at all later times, on a three-dimensional hypersurface in six-dimensional phase-space. This hypersurface is usually referred to as the phase-space sheet (48). A consequence is that the velocity spectrum at any point in physical space is discrete, i.e., at every point in physical space there is a discrete set of axion dark matter flows, each flow corresponding to a particular way cold axions can reach that location from the far past. The number of flows at a given physical location is the number of times the phase-space sheet covers three-dimensional physical space there. At the boundaries between regions in physical space with differing number of flows, the phase-space sheet is tangent to velocity space. As a result, the dark matter density is very large on these surfaces, which are termed caustics (49). The density diverges at the caustics in the limit of zero velocity dispersion. Sikivie (50) claimed, on the basis of theoretical studies and observational evidence, that Earth is located close to a dark matter caustic in the Milky Way halo and that, as a result, the local dark matter distribution is dominated by a single flow of known velocity vector.

Finally, there is a particular kind of clumpiness (36, 51) that affects axion dark matter if there is no inflation after the PQ phase transition. This is due to the fact that the dark matter axions are inhomogeneous with $\delta\rho/\rho \sim 1$ over the horizon scale at temperature $T_1 \simeq 1$ GeV, when they are produced at the start of the QCD phase transition, combined with the fact that their velocities are so small that they

do not erase these inhomogeneities by free streaming before the time t_{eq} of equality between the matter and radiation energy densities when matter perturbations can start to grow. These particular inhomogeneities in the axion dark matter are in the nonlinear regime immediately after time t_{eq} and thus form clumps, termed axion mini-clusters (51). They have mass $M_{mc} \simeq 10^{-13} M_{\odot}$ and size $l_{mc} \simeq 10^{13}$ cm.

5. LIMITS ON THE AXION

This section summarizes the principal experiments and observations that limit the mass of the axion and its coupling to photons. An exhaustive discussion of the qualifications and uncertainties of the mass limits in particular is beyond the scope of this review, but are dealt with systematically in References 9–11. Bear in mind that the various upper limits on the axion mass are always derived from experiments or observations through specific couplings, i.e., ANN, $A\gamma\gamma$, Aee, and thus are implicitly dependent on the specific axion model.

5.1. Laboratory Experiments Through Axion-Photon Mixing

The propagation of light through a magnetic field is affected by higher-order QED light-by-light scattering, which induces a birefringence of the vacuum (Figure 3). Axions further modify QED, as they can mix with photons in an external electromagnetic field. The interaction of axions and photons in an external magnetic field is given by $\mathcal{L}_{int} = g_{A\gamma\gamma} A\mathbf{E} \cdot \mathbf{B}$; thus, a photon traveling through a transverse magnetic field will have a probability of oscillating into the axion state (real or virtual), and vice versa. Axion-photon mixing thus makes possible sensitive searches for the axion utilizing lasers and high-energy physics dipole magnets. The formalism of higher-order QED, axion-photon mixing, and medium effects are presented in the section on solar axions (see Section 7). Here we simply discuss experimental results enabled by mixing.

5.1.1. PHOTON REGENERATION: SHINING LIGHT THROUGH WALLS Figure 4 shows the concept of photon regeneration (52, 53), whereby a laser beam is directed through a dipole magnet polarized parallel to the field. The probability for axion-photon conversion is given by $\Pi = (\omega/4k_A)(gB_0l)^2F^2(q) \approx (1/4)(gB_0l)^2$ for $q \ll l^{-1}$, where l is the length of the magnet and B_0 is its strength; here, $g = g_{A\gamma\gamma}$ for simplicity. As the axion is massive $[k_A = (\omega^2 - m_A^2)^{1/2}]$, whereas the photon is massless ($k_\gamma = \omega$), there is a momentum mismatch, $q \equiv k_\gamma - k_A \approx m_A^2/2\omega$ for $m_A \ll \omega$, thus defining the oscillation length in the problem. $F^2(q)$ is the square of the Fourier transform of the magnetic-field profile in z, normalized to unity for $q = 0$. Axions produced in the first magnet pass through a brick wall and reconvert to photons with the same probability. As the probability for conversion and reconversion $P(\gamma \to A \to \gamma) = \Pi^2 \propto g^4$, the sensitivity to g scales linearly with B_0l, but only poorly with laser power and counting time. Such an experiment

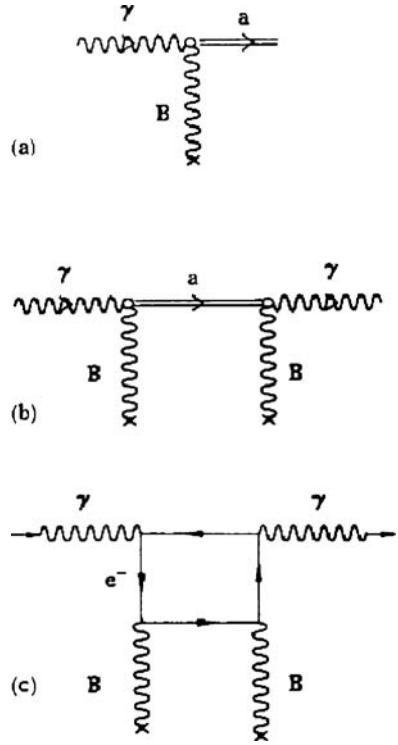

Figure 3 Axion-photon mixing and higher-order QED relevant to the axion searches described in this review. (*a*) Processes at the heart of dark matter axion and solar axion detection. It also results in dichroism (rotation of the plane of polarization) in photon regeneration experiments. (*b*) Another process involving the axion that produces birefringence (change in ellipticity) in the polarization experiments. (*c*) A QED process not involving the axion that likewise produces birefringence in polarization experiments.

has been carried out by Ruoso et al. (54), using two Brookhaven colliding beam accelerator (CBA) dipoles (each 4.4 m long, 3.7 T) and an argon ion laser (1.5 W, 200 traversals in an optical cavity). A limit of $g < 7.7 \times 10^{-7}$ GeV was established for $m_A < 10^{-3}$ eV.

5.1.2. POLARIZATION EFFECTS Another manifestation of the axion would be in the change of polarization of light traveling through a magnetic region. Linearly polarized light is injected into an optical cavity within the magnet with the electric-field vector **E** at some nonzero angle φ with respect to the **B** field (optimally 45°) and later extracted and analyzed for a change in its polarization state. The optical cavity allows the signal to build up by a factor N, the number of reflections in the cavity. Figure 3 shows three diagrams that contribute to this change in polarization.

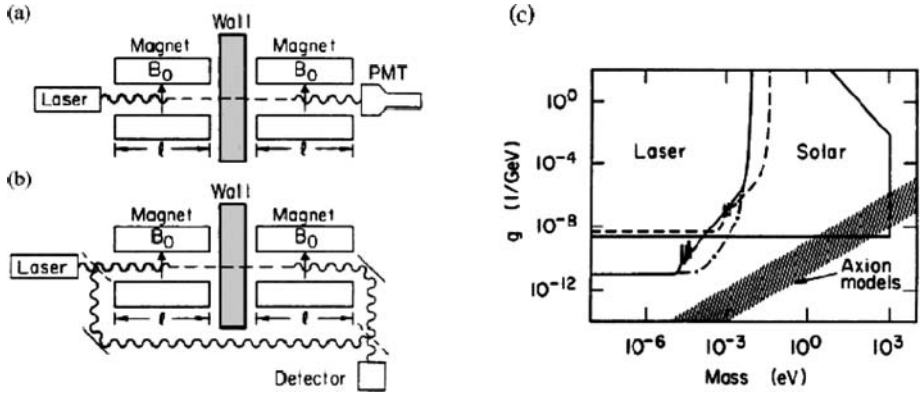

Figure 4 (*a*) The photon regeneration experiment. (*b*) Homodyning, which eliminates the dependence of the sensitivity of the experiment on any external source of noise. (*c*) Sensitivity of the experiment for various configurations. (*Dashed line*) 10 T–10 m magnet, 1 kW optical laser. (*Solid line*) 30 SSC dipoles per leg (6.6 T–16.6 m), 100 kW CO2 laser. (*Dot-dashed line*) Same as the solid line, but a wiggler geometry, i.e., alternating polarity of magnets to maximize $F^2(q)$ as far out in mass as possible. Figure taken with permission from Reference 53.

Figure 3*a* represents the production of real axions, which, because it depletes photons in the cavity, is equivalent to an imaginary component of the index of refraction of the vacuum for one polarization state. As only the $E_\parallel$ component can produce axions, $E_\parallel$ is foreshortened by a tiny amount, whereas $E_\perp$ is not, leading to a rotation of the linearly polarized light. Figures 3*b* and 3*c* both lead to a birefringence of the vacuum or to linearly polarized light becoming elliptically polarized. Figure 3*c* is the light-by-light scattering diagram seen in Delbrück scattering and measured in the muon $(g-2)$ experiment, producing indices $n_\perp = 1 + (4/2)\xi$, $n_\parallel = 1 + (7/2)\xi$, where $\xi = \alpha/45\pi(B_{ext}/B_{crit})^2$ and $B_{crit} = m_e^2/e \approx 4.4 \times 10^{13}$ Gauss.

The Rochester-Brookhaven-Fermilab (RBF) collaboration performed such an experiment with two CBA superconducting dipoles end to end (8.8 m, $\langle B^2\rangle = 4.5T^2$) and an optical cavity that allowed the laser beam to make ~ 500 passes through the magnet to build up the signal (55). Ultimately, the experiment demonstrated sensitivity to an optical rotation of $\epsilon = 0.38 \times 10^{-9}$ and an ellipticity of $\Psi = 2 \times 10^{-9}$. Although an experimental tour de force, nevertheless, the predicted effect from QED for this experiment was $\Psi^{QED} = 4.7 \times 10^{-13}$, and from a standard axion ($g \approx 10^{-13}$ GeV^{-1} at $m_A \approx 1$ meV) $\Psi^A = 3 \times 10^{-22}$. Figures 5*a* and 5*b* display the limits the RBF results cast on the coupling of a generalized pseudoscalar versus mass. The PVLAS collaboration has recently mounted a more sensitive experiment, with a high-finesse Fabry-Perot cavity encompassing the dipole-field region (56). They report a positive polarization rotation

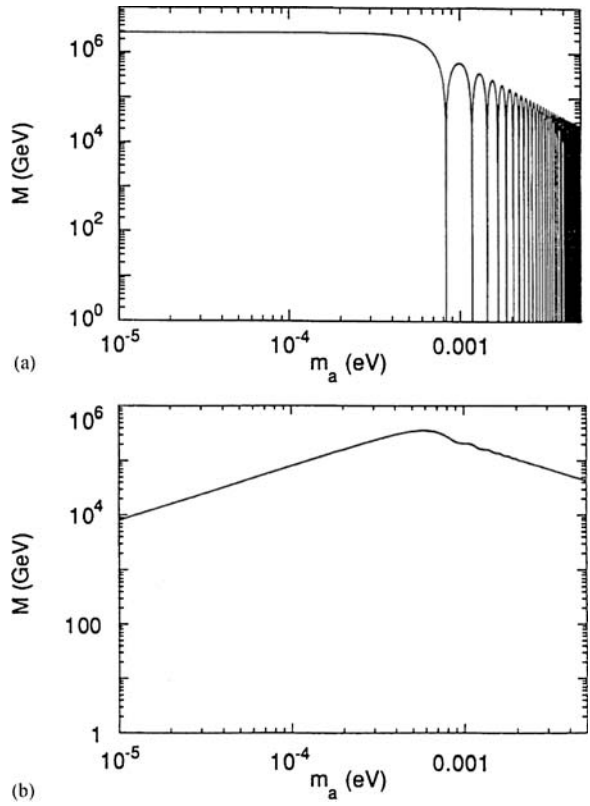

Figure 5 Limits on the coupling to photons of an axion-like particle (here $M \equiv g^{-1}$) from (*a*) polarization and (*b*) ellipticity (55).

signal, corresponding to a rotation of $(3.9 \pm 0.5) \times 10^{-12}$ rad per pass through the magnet (1 m, 5 T). If interpreted as a light pseudoscalar, the measured rotation is consistent with the previous RBF results, so long as the mass is in the 1–1.5 meV range, and $M \equiv g^{-1} = (2 - 6) \times 10^5$ GeV. How to reconcile this result with the much more stringent astrophysical limits is beyond the scope of this review.

5.2. Astrophysical and Cosmological Limits

The present mass limits on the axion result from considerations other than laboratory experiments. Astrophysics establishes the upper bound on the axion mass by arguments based on the effect of axion production in stellar evolution. The various stellar exclusion regions form a seamless cloth from accelerator bounds down to the milli-electronvolt range. Cosmology provides the lower bound by overclosure arguments.

5.2.1. ASTROPHYSICAL LIMITS Axions, as well as other low-mass weakly interacting particles, are produced in the hot and dense astrophysical plasmas, carrying away energy directly from the interior of stars. Various astronomical observables constrain the strength of the axion interaction with photons (as well as with electrons and nucleons). The most restrictive limit arises from the evolution of horizontal-branch (HB) stars, where axion emission reduces the helium-burning lifetime, i.e., the observed number ratio of HB stars in globular clusters. The adopted limit (57) on the axion-photon coupling constant is

$$g_{A\gamma\gamma} \lesssim 11.0 \times 10^{-10}\ \mathrm{GeV}^{-1}. \qquad 8.$$

(A slightly more restrictive limit may be obtained by using 10% precision for the helium-burning lifetime.)

For comparison, the evolution of the sun, i.e., the age of the solar system, provides a limit for the axion-photon coupling constant

$$g_{A\gamma\gamma} \lesssim 2.3 \times 10^{-9}\ \mathrm{GeV}^{-1}, \qquad 9.$$

whereas helioseismology improves this limit further (58):

$$g_{A\gamma\gamma} \lesssim 1.0 \times 10^{-9}\ \mathrm{GeV}^{-1}. \qquad 10.$$

Note that the new cosmologically derived, hadronic axion-rest-mass limit (59) is $m_A < 1.05$ eV (95% C.L.). This suggests extending the axion searches, such as the one undertaken by the CERN Axion Telescope (CAST) experiment at CERN, into the ~eV rest-mass range.

5.2.2. COSMOLOGICAL LIMITS As discussed in greater detail in Section 4.1, the energy density of axions generated during the Big Bang increases for axions of smaller mass. This is a general feature, independent of the exact mechanism, whether it be vacuum realignment or string radiation. The sum of contributions from vacuum realignment, string decay, and wall decay yields a total cold axion energy density on the order of $\Omega_A \approx (0.1 \text{ to } 10)\ (\frac{\mu\mathrm{eV}}{m_A})^{7/6}$, depending on whether inflation occurs with reheat temperature lower or higher than the PQ transition temperature (see Section 4.1). A precision measurement of cosmological parameters yields $\Omega_{CDM} \approx 0.22$ (60), implying a lower limit on the axion mass on the order of 0.5 μeV, with however large uncertainties.

6. SEARCHES FOR COSMOLOGICAL AXIONS

6.1. The Microwave Cavity Experiment

The microwave cavity technique is premised on Sikivie's (6) proposal to resonantly stimulate axion-to-photon transitions in a background magnetic field of strength B_0. In practice, a high-Q cavity is placed in a large magnetic field and conversion is enhanced enormously by both the increased density of states around

the final photon frequency and the virtual photons supplied by the external field. Resonant conversion of axions comprising our galactic halo occurs when the cavity frequency equals m_A. The corresponding power on-resonance is given by (6)

$$P_A = \left(\frac{\alpha}{\pi}\frac{g_\gamma}{f_A}\right)^2 V B_0^2 \rho_A C \frac{1}{m_A} \mathrm{Min}(Q_L, Q_A)$$

$$= 0.5 \times 10^{-26} \mathrm{watt} \left(\frac{V}{500\ \mathrm{liter}}\right)\left(\frac{B_0}{7\ \mathrm{tesla}}\right)^2 C \left(\frac{g_\gamma}{0.36}\right)^2$$

$$\times \left(\frac{\rho_A}{\frac{1}{2} \times 10^{-24} \frac{g}{\mathrm{cm}^3}}\right)\left(\frac{m_A}{2\pi(\mathrm{GHz})}\right) \mathrm{Min}(Q_L, Q_A), \qquad 11.$$

where V is the volume of the cavity, B_0 is the magnetic-field strength, Q_L is its loaded quality factor, $Q_A = 10^6$ is the quality factor of the galactic halo axion signal (i.e., the ratio of their energy to their energy spread), ρ_A is the density of galactic halo axions at Earth, and C is a mode-dependent form factor given by

$$C = \frac{\left|\int_V d^3x \vec{E}_\omega \times \vec{B}_0\right|^2}{B_0^2 V \int_V d^3x \epsilon |\vec{E}_\omega|^2}, \qquad 12.$$

where $\vec{E}_\omega(\vec{x})e^{i\omega t}$ is the oscillating electric field of the mode in question and ϵ is the dielectric constant. Only cavity modes in which the electric field is substantially parallel to the external magnet field satisfy the Lagrangian in Equation 4. For a cylindrical cavity and a homogeneous longitudinal magnetic field, $C = 0.69$ for the TM_{010} mode. The form factors of the other TM_{0n0} modes are much smaller, and form factors for pure TE, TEM, and the remaining TM modes are zero. Even when combining the strongest magnets and highest-Q cavities available, the expected signal is extraordinarily weak owing to the extremely small coupling between the axion and the photon. For this reason, to detect a signal, the cavity's physical temperature and equivalent electronic noise temperature must be as low as practical.

The well-known Dicke radiometer equation specifies the time required to achieve a given signal-to-noise ratio (SNR) as

$$SNR = \frac{P_A}{P_n}\sqrt{Bt} = \frac{P_A}{k_B T_n}\sqrt{\frac{t}{B}}, \qquad 13.$$

where P_n is the average thermal power, T_n is the sum of the physical temperature of the cavity plus the noise temperature of the microwave receiver that detects the photons, and B is the bandwidth.

Because the axion mass is unknown, a crucial element to any search experiment is tunability. Incremental changes in cavity frequency are achieved by moving

metallic or dielectric tuning rods. For a fixed SNR, the maximum scan rate is given by

$$\frac{df}{dt} = \frac{12\text{GHz}}{\text{year}}\left(\frac{4}{\text{SNR}}\right)^2\left(\frac{V}{500\text{ liter}}\right)^2\left(\frac{B_0}{7\text{ tesla}}\right)^4 C^2\left(\frac{g_\gamma}{0.36}\right)^4$$
$$\times\left(\frac{\rho_A}{\frac{1}{2}\times 10^{-24}\frac{g}{\text{cm}^3}}\right)^2\left(\frac{3K}{T_n}\right)^2\left(\frac{f}{\text{GHz}}\right)^2\frac{Q_L}{Q_A}. \quad 14.$$

Equations 11 and 13 dictate the nature of the search strategies. The large allowed mass range and absence of a broadband search technique preclude exploiting B or t in Equation 13, thus shifting the emphasis to the remaining parameters accessible to experimenters: T_n, B_0, or V. For reasons that are made clearer in subsequent sections, a great deal of effort has gone into reducing T_n and, hence, improving the scan rate.

6.2. Previous Experiments

Shortly after the publication of the cavity haloscope proposal (6), two small proof-of-principle experiments got underway, one by a RBF collaboration (61, 62), and the other by a group at the University of Florida (UF) (63). It is a tribute to these two efforts that the design and operational strategy of the current Axion Dark Matter eXperiment (ADMX) in the United States, and to a lesser degree Cosmic Axion Research using Rydberg Atoms in a Resonant Cavity in Kyoto (CARRACK) in Japan, have carried over directly from their work.

The RBF and UF experiments were very similar in their scale and design, utilizing superconducting magnets and right-circular, copper microwave cavities up to 15 cm in diameter and 40 cm in length (the RBF apparatus is shown in Figure 6). Both employed heterojunction field-effect transistor (HFET) amplifiers with noise temperatures of 5–20 K, with the cavity and amplifier cooled to either liquid helium temperature (4.2 K) or pumped liquid helium (1.3 K) temperature. A noteworthy feature of the RBF experiment was the detailed circuit modeling of the coupled cavity and receiver (64). The UF effort produced a detailed study of microwave cavity resonators for the dark matter axion experiment (65), including modeling and demonstrating the utility of power-combining multiple cavities for operation at higher frequencies (66). Remarkably, in spite of cavity volumes of only a few liters, both RBF and UF set exclusion limits in $g^2_{A\gamma\gamma}$ within two to three orders of magnitude of the model band, in the mass range of 4.5 to 16.3 μeV (1.09 to 3.93 GHz) (Figure 7).

6.3. The Axion Dark Matter eXperiment

A collaboration of U.S. institutions (currently LLNL, UF, UC Berkeley, and NRAO) has built the next generation of microwave cavity experiments, whose scientific goal is to cover the 1–10 μeV mass range, with sensitivity to the KSVZ

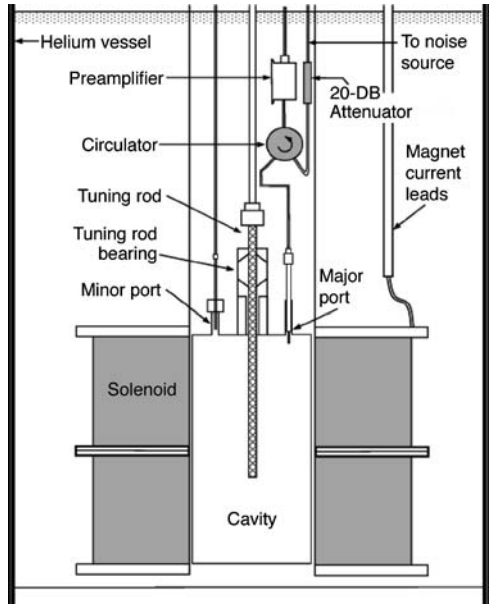

Figure 6 Schematic of the Rochester-Brookhaven-Fermilab microwave cavity dark matter axion detector (62).

axion models. Known as the ADMX, the gain in sensitivity was predicated upon a scale-up of the active volume of the experiment and projected improvements in the effective noise temperature of the microwave amplifier. The experiment began operation in 1996 and covered nearly an octave in frequency range, between 450–810 MHz (1.86–3.36 μeV), before shutting down in 2004 for an upgrade.

A schematic of the experiment is shown in Figure 8. A single copper-plated stainless-steel cavity of 1 m long $\times$ 0.5 m in diameter is inserted within the NbTi superconducting solenoidal magnet of 8.5 T central field. Radial translation of metal (copper) and dielectric (alumina) tuning rods within the cavity allow a roughly $\pm$50% tuning range, without undue loss of quality factor, which is on the order of the theoretical maximum allowed by the anomalous skin depth, $Q \sim 10^5$. A brief run with an array of four-cavities was carried out to establish the feasibility of multicavity operations reaching higher frequencies (69).

Power from the TM_{010} mode of the cavity is extracted by a stub antenna and coupled to an HFET amplifier. Steady progress in HFET devices and amplifier packaging by NRAO has resulted in dramatic improvements in their equivalent noise temperature (13); amplifier noise in the gigahertz region has reached 1–1.5 K, yielding a system noise temperature of $T_s = T + T_n \approx 1.3 + 1.5 < 3$ K. A double heterodyne receiver mixes the signal twice down to the audio frequency range, and

the power spectrum is calculated in hardware by a Fast Fourier Transform (FFT) routine. The receiver output is actually split, with one leg dedicated to the medium-resolution channel, the other to a high-resolution channel. The medium-resolution channel calculates the power spectrum in bins of $\Delta\nu/\nu \approx 10^{-7}$, appropriate to resolve the virialized component of halo axions, whereas the high-resolution channel calculates the power spectrum in bins of $\Delta\nu/\nu \approx 10^{-11}$ to search for possible fine structure in the signal (refer to Section 4.2).

A 50-kHz-wide medium-resolution subspectrum is integrated for 80 seconds, after which time the central cavity frequency moves ~2.5 kHz. Owing to one or more passes over the same frequency range, each frequency bin appears in 40–60 subspectra, from which the final power spectrum is computed by co-adding the subspectra with appropriate weighting. The group has shown that fluctuations in the power spectrum continue to fall as $t^{-1/2}$, in accord with the radiometer equation for integration times of one month before receiver systematics limit further decrease. This implies an ultimate spectral sensitivity in this experiment of 10^{-26} watts; thus, in principle, a signal of only one additional RF photon per minute could be detected above the blackbody and electronic noise (70).

The data analysis proceeds by a hierarchical procedure of threshold cuts and rescans of persistent peaks in the Gaussian noise spectrum. Ultimately, a tractable number of candidate peaks remain for examination. Peaks that are statistical fluctuations ultimately disappear upon repeated integration; environmental (radio) peaks are identified using a variety of techniques, such as terminating inputs to the cryostat. No axion candidate has survived so far, and KSVZ axions have been excluded at the 90% C.L., for the maximum-likelihood halo density of 0.45 GeV cm^{-3}, as shown in Figure 9*a* (70). Figure 9*b* shows the excluded halo density, assuming KSVZ axions (71).

This collaboration has also recently performed a high-resolution analysis over a limited mass range, and demonstrated greatly enhanced reach in $g_{A\gamma\gamma}$, under the assumption that the axion signal contains one or more fine-structure peaks owing, e.g., to late-infall axions (72). Confidence in this analysis is supported by quantitatively correlating the same environmental (radio) peaks in both the medium-resolution and high-resolution spectra, the latter deriving from a ≈50-second-long FFT at each frequency setting (Figure 10). Note that this experiment is very nearly sensitive to DFSZ axions, under the assumption that the estimated halo density is dominated by a single cold flow. Should the axion ever be discovered and found to possess fine structure, the diurnal and sidereal modulation of the frequency of the peaks would provide a wealth of information on the structure and history of the formation of our galaxy.

From the radiometer Equation 13, one may derive two scaling laws critical to the microwave cavity experiment. First, for a search conducted to scan the mass range at a constant value of the axion-photon coupling constant, $g_{A\gamma\gamma}$, the frequency scan rate goes as $(1/\nu)(d\nu\ dt) \propto (B^4V^2)T_s^{-2}$, where T_s is the total system noise temperature. Second, for a search conducted at a constant scan rate, the power sensitivity goes as $g_{A\gamma\gamma}^2 \propto (B^2V)^{-1}T_s$. These underscore the importance

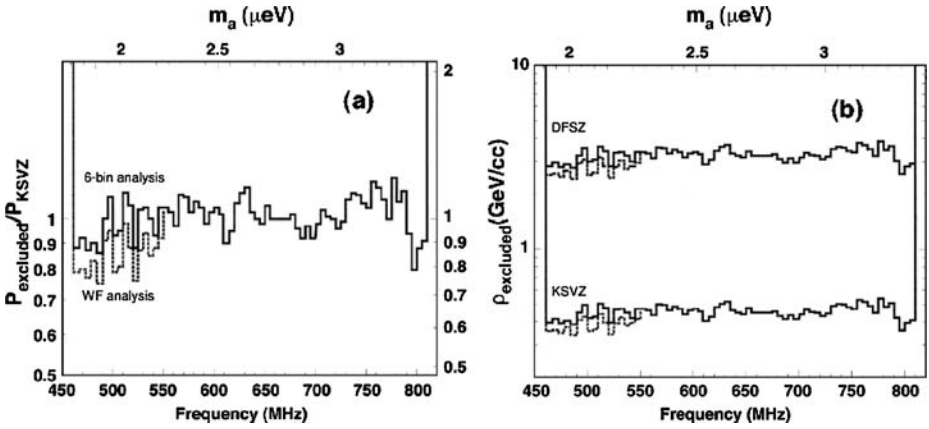

Figure 9 Exclusion limits (90%) by Axon Dark Matter eXperiment for (*a*) the axion-photon coupling $g_{A\gamma\gamma}$, assuming the maximum-likelihood estimate of the dark matter halo density (70), and (*b*) the halo density ρ_A, assuming KSVZ axions (71).

of reducing the system noise temperature, the sum of the physical plus amplifier temperatures, as the most practical way to cover the parameter space in both coupling and mass. In the case of ADMX, there is still much room for improvement, as the theoretically irreducible noise of a device, i.e., the standard quantum limit, $kT_n \approx h\nu \approx 50$ mK at 1 GHz, whereas the best system noise temperature currently is on the order of 3 K. SQUIDs (Superconducting Quantum Interference Devices) have long been used as ultra-sensitive magnetometers and ultra-low-noise amplifiers in the quasi-static regime, but until recently had never been used as high-gain amplifiers above 100 MHz. Motivated by the microwave cavity axion experiment, in the late 1990s Clarke and coworkers (73) at UC Berkeley achieved a breakthrough in SQUID design and fabrication, which allowed SQUIDs to be configured as high-gain ultra-low-noise gigahertz amplifiers. At the heart of the design was a new way of coupling the input signal to the SQUID loop, i.e., through a microstrip line (Figure 11*a*) (73). Resonant microstrip-line coupling circumvented the limitation of the old Ketchen-type SQUID, namely the parasitic capacitance between the input primary coil and the SQUID loop that would increasingly shunt the signal to ground at higher frequencies. Among other features of the microstrip-coupled DC SQUID, this group demonstrated how, although being a narrow-band resonant device, the microstrip SQUID could be tuned in situ a factor of two in frequency (74), making it practical for use in the dark matter axion experiment. Currently, the microstrip-coupled SQUID amplifiers are approaching the standard quantum limit in noise in the 0.5–1 GHz range (Figure 11*b*), and the microstrip design has worked up to 3 GHz. (For a summary of the DC SQUID and a complete bibliography of the microstrip-coupled SQUID, see Reference 13.)

At present, ADMX is undergoing an upgrade to incorporate packaged gigahertz DC SQUID amplifiers into the experiment. Initially, the experiment will continue to operate at pumped helium temperature, $\approx$1.3 K, and thus the total system temperature will improve by only a factor of two or so. After a period of data taking in the 800–1000 MHz range, a second upgrade is planned to retrofit the experiment with a dilution refrigerator; the total system noise temperature at that point should be on the order of 100–200 mK. This will enable the experiment to exclude DFSZ axions, even at densities much less than the maximum-likelihood halo estimate, while also permitting an appreciable improvement in the rate of frequency coverage. Microwave resonator and amplifier concepts need to be developed for the search to proceed to the 10–100 μeV range; even concepts for the third decade in open mass range, i.e., 100 μeV to 1 meV are lacking.

6.4. The Cosmic Axion Research Using Rydberg Atoms in a Resonant Cavity in Kyoto

The ADMX in the United States and its predecessors benefited from the steady improvements over years of development in noise temperature of conventional HFET amplifiers. The upgrade of ADMX with DC SQUID amplifiers will ultimately run into a fundamental limiting noise temperature, the so-called standard quantum limit, $T_N \approx h\nu/k_B$, where k_B is the Boltzmann constant. A discussion of generalized amplifiers and quantum noise is beyond the scope of this review, but an accessible treatment of the essentials as they pertain to the microwave cavity experiment can be found in a recent report (13). The origin of the quantum limit is the uncertainty principle between the number and phase of photons measured in a radiation field, $(\Delta n)(\Delta\phi) > 1$ (75). Every real device, i.e., an amplifier or some other detector, is situated somewhere within a continuum, in which one extreme treats the photon as a wave (maximum number uncertainty) and the other extreme treats the photon as a particle (maximum phase uncertainty). A classical amplifier is subject to the standard quantum limit.

A parallel dark matter axion program, which has pursued the latter strategy as a counterpoint to U.S. efforts, has been ongoing in Japan for more than a decade. Whereas the front end of the experiment is the same Sikivie microwave cavity apparatus, the back end replaces the microwave amplifier with a Rydberg-atom single-quantum detector. This section describes the Rydberg-atom technique, the CARRACK1 prototype detector, and first results demonstrating that blackbody photons can be counted well below the temperature corresponding to the standard quantum limit.

6.4.1. RYDBERG-ATOM SINGLE-QUANTUM DETECTION Atoms with a single electron promoted to a very high principal quantum number ($n \gg 1$) can be expected to have quasi-hydrogenic properties, but also exhibit fascinating semiclassical behavior. The invention of the laser, and in particular the tunable dye laser, enabled intensive investigation of their properties and spectroscopy. Kleppner (76) first

recognized the potential application of Rydberg atoms for single-photon counting in the microwave regime; this observation was based on three specific characteristics. First, owing to their size, the electric dipole moment between adjacent levels $\langle n+1|e\mathbf{r}|n\rangle \propto \tilde{n}^2$, and thus the atom's coupling to radiation fields, can be very large. (The effective principal quantum number, $\tilde{n} = n - \delta_\ell$, incorporates the shielding of the nucleus by the core electrons through the quantum defect parameter, δ_ℓ.) Second, transitions between Rydberg states, $\Delta E_n = E_{n+1} - E_n \approx 2\mathcal{R}/\tilde{n}^3$, span the microwave range, e.g., $\Delta E_{100} \approx 7$GHz. Third, the states have long lifetimes: $\tau_n \propto \tilde{n}^3$, ($l \ll n$), and $\tau_{100} \approx 1$ msec. Such long lifetimes enable one to prepare highly excited states and manipulate them in atomic-beam geometries. Gallagher (77) has produced a complete and authoritative discussion of Rydberg-atom spectroscopy and phenomenology.

The implementation of the Rydberg-atom single-quantum detector in the microwave cavity experiment is shown in Figure 12. Here, in addition to the conversion cavity, there is a second (detection) cavity coupled to it; the two are kept locked together in frequency. An atomic beam, e.g., ^{85}Kr, is doubly optically pumped to a suitable Rydberg level, e.g., $|111s_{1/2}\rangle$, which then traverses the detection cavity. A parallel-plate configuration (not shown) within this cavity enables Stark tuning of the splitting of the $|111p_{3/2}\rangle$ and $|111s_{1/2}\rangle$ levels to match the cavity frequency. As the cavity and atom constitute a coupled system, photons in the detection cavity efficiently drive the $|ns\rangle \rightarrow |np\rangle$ transition. The atomic beam exiting the detection cavity thus represents a mixed state, with all but a tiny fraction in the lower state. The beam passes through a selective-field-ionization region, essentially another parallel-plate arrangement, which superposes a determined linear potential to the Coulombic atomic potential, resulting in a tunneling barrier. As is, the energy splitting is too small to achieve selective ionization of the $|np\rangle$ without appreciable tunneling leakage of the $|ns\rangle$ state, which would result in a large noise background. However, sophisticated techniques have been developed to enhance the SNR (78, 79). By applying a time-dependent electric field that affects a series of adiabatic and diabatic crossings, the two levels are mixed into an intervening manifold (i.e., a large number of degenerate high-l states) and driven apart in energy. The $|np\rangle$ state, which is transferred to the reddest (lowest) manifold state, tunnels at a much lower voltage than the $|ns\rangle$ state, which is transferred to the bluest (highest) manifold state. The resulting ionization is highly selective, with near-unit probability of ionizing the $|np\rangle$ state and negligible contamination from the $|ns\rangle$ state. The Kyoto group recently measured blackbody photons in the CARRACK1 apparatus as a function of physical temperature, and the agreement with theory is excellent (Figure 13) (80). The lowest temperature data point, 67 mK, is almost a factor of two lower than the standard quantum limit corresponding to the cavity frequency ($\sim$120 mK at 2527 MHz). This group has performed a search for axions within a range of approximately 10% in frequency with this cavity, but results are as yet unpublished. A larger version, CARRACK2, comparable in size to ADMX, has been constructed; it has been designed to be cooled to physical temperatures as low as 10–15 mK.

7. SEARCHES FOR SOLAR AXIONS

Axions should be copiously produced inside the hot solar core. In this section we present a few experiments that search for axions from the sun. Note that photon regeneration and vacuum birefringence laboratory experiments require no astrophysical or cosmological axion sources (see References 12, 81, and 56), and therefore they are complementary approaches for this field.

7.1. Solar Production of Axions

Stars can produce axions by coupling thermal photons to the fluctuating electromagnetic field of the stellar plasma (82, 83) and can be converted back into photons in the presence of a magnetic field. The formalism of the axion-photon mixing has been worked out in Reference 84. The coupling of these two processes as shown in Figure 3 is the working principle of an axion helioscope. The axion flux from the sun would be enormous compared with anything that could be produced in the laboratory for standard QCD axions.

Solar axions have a broad energy spectrum on the order of the temperature in the solar core. The expected solar axion flux at Earth due to the Primakoff process is $\Phi_A = g_{10}^2\ 3.67 \times 10^{11}\ \mathrm{cm}^{-2}\ \mathrm{s}^{-1}$, where $g_{10} \equiv g_{A\gamma\gamma} 10^{10}$ GeV, with an approximately thermal spectral distribution given by (Figure 14)

$$\frac{d\Phi_A}{dE_A} = g_{10}^2\ 3.821 \times 10^{10} \frac{(E_A/\mathrm{keV})^3}{(e^{E_A/1.103\ \mathrm{keV}} - 1)}\ \mathrm{cm}^{-2}\ \mathrm{s}^{-1}\ \mathrm{keV}^{-1}, \qquad 15.$$

and an average energy of 4.2 keV. This spectrum, first derived in Reference 85, has been reevaluated in Reference 86 with a modified normalization constant to match the total axion flux predicted by a more recent solar model. However, the possible flux variations due to solar-model uncertainties are negligible. Axion interactions other than the two-photon vertex, such as Compton-like scattering, provide for additional production channels, but in the most interesting scenarios these channels are severely constrained, leaving the Primakoff effect as the dominant channel (83). In any case, it is conservative to use the Primakoff effect alone when deriving limits on $g_{A\gamma\gamma}$.

Note that the axion flux given by Equation 15 applies strictly to axion energies far above $\hbar\omega_{plasma} \approx 300$ eV (ω_{plasma} is the plasma frequency of the solar core). No axions are emitted with energy below the $\hbar\omega_{plasma}$ because there are no initial photons inside the solar core with energy below this cutoff. It would be useful to obtain the modification of the solar axion flux due to plasma effects in the solar core. However, such a calculation is beyond the scope of this review.

7.2. Principle of Detection: Axion-Photon Mixing

A solar axion will couple to a virtual photon produced by a laboratory magnet, generating a real photon via the Primakoff effect: $A + \gamma_{virtual} \rightarrow \gamma$. Because any

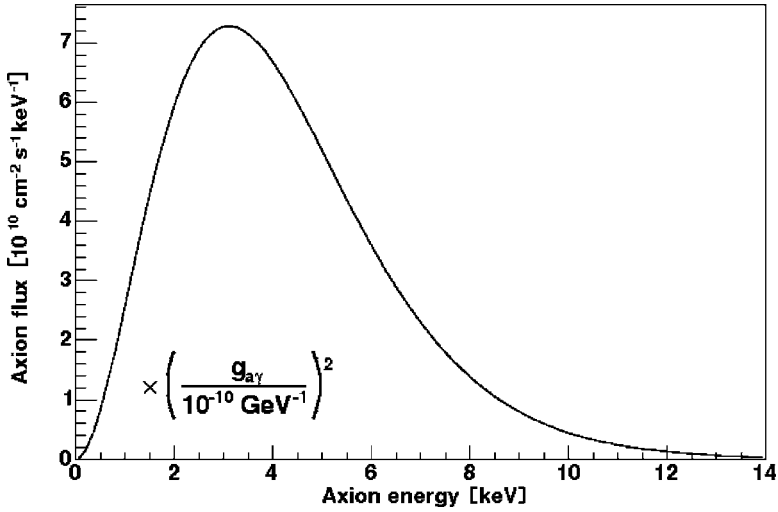

Figure 14 The solar axion flux spectrum at Earth (85).

magnetic field is sufficiently homogeneous on the length scale set by the de Broglie wavelength of solar axions, the resulting photon is collinear with the incoming axion. It is this kinematical constraint that allows a magnet to operate as an axion telescope. In addition, the energy of this photon is also equal to the axion's total energy, provided the magnetic field is time independent. The expected number of photons from converted solar axions is

$$N_\gamma = \int \frac{d\Phi_A}{dE_A} P_{A\to\gamma} S T dE_A, \qquad 16.$$

where $d\Phi_A/dE_A$ is the axion flux at Earth as given by Equation 15, S is the magnet bore area (cm^2), T is the measurement time (s), and $P_{A\to\gamma}$ is the axion-to-photon conversion probability.

In vacuum, the conversion probability of an axion to photon is given by (6, 53, 84)

$$P_{A\to\gamma} = \left(\frac{B g_{A\gamma\gamma}}{2}\right)^2 2L^2 \frac{1-\cos(qL)}{(qL)^2} \qquad 17.$$

$$\approx \frac{1}{4}(g_{A\gamma\gamma} BL)^2, \qquad 18.$$

where B is the magnetic-field component transverse to the direction of the collinear axion and photon, L is its length, and $q = k_\gamma - k_A = E_A - \sqrt{(E_A^2 - m_A^2)} \simeq m_A^2/2E$ is the longitudinal momentum difference between the axion and the X ray of energy E (the momentum transferred to the virtual photon in the

axion-photon oscillation) (84). The conversion process is coherent when the axion and the photon fields remain in phase over the length of the magnetic-field region. The coherence condition states that $qL \leq \pi$ (87, 88). For example, to have a coherence length of 10 m in vacuum requires $m_A \lesssim 0.02$ eV for a mean solar axion-photon energy of 4.2 keV. For full coherence, the latter expression is a suitable approximation.

7.3. The Axion Helioscope

The pioneering implementation of the axion-helioscope concept was performed at Brookhaven National Laboratory (87). More recently, the Tokyo axion helioscope (89) with $L = 2.3$ m and $B = 3.9$ T provided new results (90). The third-generation CAST experiment at CERN is described more in detail below. It is worth mentioning that if a signal is found because of axions, such an axion telescope provides a unique perspective for the study of the solar interior with unprecedented accuracy. This is owing to our ability to measure the energy and direction of the conversion X ray with great precision, building on technology borrowed from X-ray astronomy.

A schematic view of an axion helioscope is shown in Figure 15. Its three main parts are a superconducting dipole magnet, a tracking system, and the X-ray detectors.

7.4. The CERN Axion Telescope

To detect solar axions directly or to improve, at least, the existing limits on $g_{A\gamma\gamma}$, an axion helioscope was built at CERN by refurbishing a decommissioned Large Hadron Collider test magnet (88), which produces a magnetic field of $B = 9.0$ T in the interior of two parallel pipes of length $L = 9.26$ m and a cross-sectional area $S = 2 \times 14.5$ cm^2. The aperture of each of the bores fully covers the potentially axion-emitting solar interior ($\sim$1/10 of the solar radius). During the first stage of operation of the CAST experiment, the magnetic-field pipes are under high vacuum (below $\sim 10^{-6}$ mbar). The magnet is mounted on a moving platform, allowing it to point at the sun for 1.5 h at both sunrise and sunset throughout the whole year. When the sun is outside the helioscope's field of view, it is used for background measurements. Figure 15 gives a schematic view of the experimental setup, showing the magnet, the platform to move it, and the working principle. The superconducting magnet operates at $\sim$1.8 K (91). The calibration of the tracking system is performed by geometric survey measurements, thus allowing the magnet to orient with a pointing precision better than 0.01° (92, 93). At both ends of the magnet, three different detectors search for excess X rays. These are a conventional time projection chamber (TPC), a smaller gaseous chamber of the Micromegas type (94), and an X-ray mirror system with a charge-coupled device (pn-CCD) (95) at its focal plane 1.7 m downstream. Both the pn-CCD and the X-ray telescope are prototypes developed for X-ray astronomy (96).

The X-ray mirror system works like two combined lenses in optics, with an efficiency of ∼33% for the expected energy spectrum. With such a configuration, axion-related X rays can produce an "axion image" of the inner sun by focusing the photons to a ∼6 mm^2 spot at the focal plane. Simultaneously, the rest of the 10 × 30 mm^2 CCD chip can be utilized to derive the background during sun tracking, which accounts for any predictable or unforeseen noise. At the time of this writing, CAST is implementing a second state-of-the art X-ray optical device with a Micromegas pixel detector at the focal plane, in order to further improve its performance. An external X-ray calibration source allows it to perform an end-to-end test of the system.

7.5. Searching for a Solar Signal

As explained above, an axion signal should appear as an excess above the background, which is mainly due to environmental radioactivity and cosmic rays (mostly secondary neutrons and γ-rays). Figures 16*a* and 16*b* show the first background-15 spectra of the TPC and Micromegas detectors, whereas Figure 16*c* gives the raw CCD data.

The intensity of the signal spectrum is proportional to $g^4_{A\gamma\gamma}$, as both axion production inside the sun and its back conversion to X rays inside the magnetic field depend on $g^2_{A\gamma\gamma}$. This is used for the fit function to the experimentally subtracted spectra, i.e., tracking spectrum minus measured background. More information on the analysis to extract a solar axion signal is given in Reference 57.

Figure 17 shows the preliminary data taken from all three detectors, with vacuum inside the magnetic pipes of the CAST magnet until 2005. For the first time the preliminary result from CAST is below the best astrophysically derived limit

$$g_{A\gamma\gamma} < 10^{-10}\ \mathrm{GeV}^{-1} \qquad 19.$$

($m_A \leq 0.02$ eV). Note that the axion signal is rest mass–independent, as the axion-photon oscillation length exceeds the length of the magnet. However, for higher m_A and vacuum inside the magnetic pipes, not only does the signal strength diminish rapidly, but the spectral shape also differs (not shown).

Furthermore, the potential of the CAST experiment to test the presence of large extra dimensions was explored in Reference 97. The high multiplicity of KK states, which gives at most one order of magnitude more stringent limit on

Figure 16 (*a*) First results from each of the CERN Axion Telescope (CAST) X-ray detectors (57), and background-subtracted spectra for time projection chamber. (*b*) Micromegas together with the expectation for the best fit $g_{a\gamma}$ (*lower curve*) and for the 95% C.L. on $g_{a\gamma}$. (*c*) The two spectra taken by the charge-coupled device tracking (*dots*) and background (*dashed line*) are also shown.

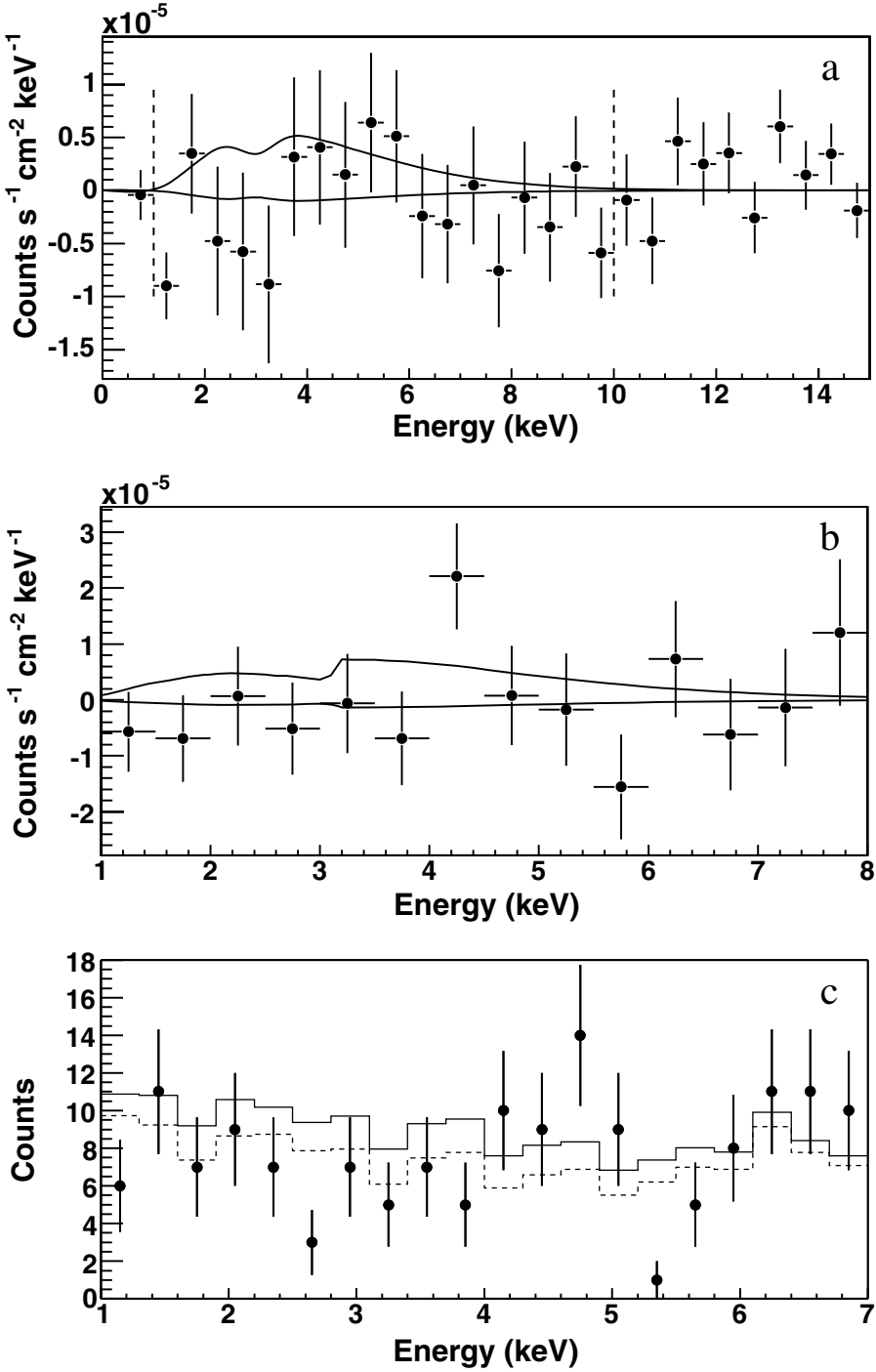

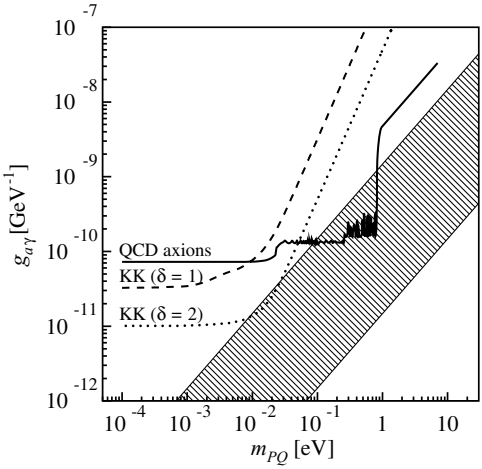

Figure 18 Limits on the axion-photon coupling as a function of the fundamental Peccei-Quinn (PQ) axion rest mass $m_{\rm PQ}$. The solid line gives the envisaged performance of CERN Axion Telescope (CAST) for quantum chromodynamics (QCD) axions (using numerical values from Reference 88). The wide, hatched region marks the (relaxed) theoretically favored region in four dimensions (brane). The dashed and dotted lines correspond to prospects of CAST for Kaluza-Klein (KK) axions in the case of two extra dimensions for $\delta = 1$ and $\delta = 2$, respectively.

the axion-photon coupling constant, is obtained using the compactification-radius limit from direct tests of gravitational-force law ($R = 0.15$ mm $\Rightarrow 1/R = 1.3 \times 10^{-3}$ eV), as shown in Figure 18. Another feature visible in Figure 18 is a strong decrease in sensitivity to $g_{A\gamma\gamma}$ for $m_{\rm PQ}R \gg 1$ as a consequence of mixing between the four-dimensional axion and the infinite tower of KK excitations (97).

An interesting feature of the CAST experiment is the coherence condition, which enables the detection and identification of KK mass states. The CAST experiment could be sensitive to the presence of two large extra dimensions, with the compactification radius as low as 370 nm or 250 nm (depending on the mass of the axion zero-mode), which is comparable to the astrophysical limits (97).

7.6. Extending the Axion-Rest-Mass Sensitivity

Coherence can be restored, e.g., for CAST, for a solar axion rest mass up to $\sim$1.2 eV by filling the magnetic conversion region with a refractive gas, e.g., helium, or better, hydrogen, owing to its smaller photoabsorption. The formalism has been worked out in Reference 85. This coherence restoration can be understood in short as follows: A gas with a given index of refraction n for the emerging X rays slows down the photon only, so that the propagation of the photon matches that of the axion inside the entire magnetic-field region, where the axion-photon oscillation occurs. In fact, the plasma frequency (ω_{pl}) of the gas defines an

effective mass (m_γ) of the photon. Coherence is restored for an axion rest mass $m_A = m_\gamma = \hbar\omega_{plasma} \approx \sqrt{4\pi r_0 \rho Z}$, which depends on the density ρ, the atomic charge Z of the gas, the classical electron radius r_0, and the length of the magnetic volume (85).

Because the axion rest mass is an unknown parameter of the theory, one has to scan many pressure settings. For an appropriate gas pressure, coherence can thus be preserved, although only for a narrow axion-rest-mass window, as is demonstrated with the resonance-like line shape in Figure 19. Thus, one can extend the search for solar axions with higher rest mass by varying the buffer-gas density inside the magnetic pipes. Should the axion be discovered in this manner, however, its mass would be determined with great precision.

This extension in axion-rest-mass sensitivity may be essential for a direct solar-axion detection. In CAST, for the first time, a laboratory experiment can search for (solar) axions in the theoretically motivated axion-rest-mass range up to ~1.2 eV (see Figure 17), which competes with the best astrophysically derived limit for the axion-interaction strength, and it is also cosmologically motivated for hadronic axions (59).

CAST Phase II is taking data with helium gas inside the 1.8-K magnetic pipes: first with low pressure ^{4}He (up to ~14 mbar, before it liquefies) and later with ^{3}He (up to ~60 mbar or higher, due to its higher vapor pressure). This will allow extending the solar axion searches, initially up to a rest mass of ~0.8 eV. Beyond this range, CAST could search for axions with still higher masses up to ~1.2 eV, but would require major modifications (T. Niinikoski & M. Davenport, private communication).

7.7. Bragg Scattering with Solar Axions

The Primakoff effect with solar axions can take place in the microscopic electric field of atomic nuclei, which provides the virtual photon for the process. This is the same mechanism assumed to give rise to axion production inside the hot stellar core. This concept exploits the coherent axion-to-photon conversion when their angle of incidence satisfies the Bragg condition with a crystalline plane (98). In fact, the ~4.2 keV mean energy of solar axions coincides with the X-ray energy chosen in conventional Bragg-scattering experiments. Thus, monocrystalline detectors (as large as ~1 kg in mass) can operate as axion telescopes thanks to the energy-angular dependence of the Bragg condition ($n\lambda = 2d \sin\theta$). The theoretical formalism is given in References 86, 99, and 100. Remarkably, the conversion process can occur coherently over the entire periodic lattice of a single crystal, which compensates for the quite large momentum difference (~1–10 keV/c) between the incoming axion and the resulting photon. This implies a diminishing momentum transfer Δp for the reaction, associated with a large wavelength that defines the coherence length. Furthermore, for a polycrystalline detector, the directionality of the process disappears along with the diminishing coherence. The detector atoms interact via the Primakoff effect with the (solar) axions, but independently of each other (i.e., incoherently).

Underground experiments like SOLAX in Sierra Grande, COSME in the Canfranc underground laboratory, and DAMA at Gran Sasso searched for solar axions in data taken with single-crystal Ge and polycrystalline NaI detectors while searching for WIMPs or other reactions (99, 101, 102). However, these limits are considerably weaker than those from the current solar helioscopes, with all results falling in the range of $g_{A\gamma\gamma} = (1.5 - 2) \times 10^{-9}$ GeV^{-1} (Figure 17).

8. CONCLUSIONS

After nearly 30 years, the PQ mechanism remains the only viable solution to the strong-CP problem, but the resulting axion has proven a formidable challenge. Nevertheless, solid progress is being made. Note that although the axion has many couplings, its induced coupling to photons has proven the most powerful (if not yet fruitful!) in terms of enabling experiments to approach realistic axion models. In fact, nearly every axion search in the past two decades has been based on the Primakoff effect, by which a pseudoscalar can convert in an external electromagnetic field to a single real photon. The sensitivity of these experiments depends on both the extremely high fields afforded by modern superconducting magnet technology and, equally importantly, the role of coherence in axion-photon mixing over large spatial volumes. This was the key insight, at least implicitly, in Sikivie's seminal paper (6), which proposed what has emerged as the two most promising avenues for the axion search: the microwave cavity search for dark matter axions and the search for solar axions. The experimental situation is summarized in Figure 20. The cavity microwave searches, which rely on the assumption that axions constitute the dark matter, have already probed well into the band of plausible axion models. With sufficient scanning time, ADMX should ultimately cover up to 10^{-4} eV or so, but the design of the resonator(s) to reach up to 25 GHz or beyond has yet to be resolved. For the decade 10^{-4}–10^{-3} eV, there are not even concepts for the cavities. The solar axion experiments are broadband in mass coverage and rely only on robust calculations of axion production from the sun's core. The third-generation experiment, CAST, has equaled and is poised to better the astrophysical bounds, specifically those from HB stars. By using a low-Z gas of tunable pressure, the axion- and photon-dispersion relations may be matched, allowing the search to push up into the O (1 eV) mass range, and thus into the space of realistic models. In principle, such axions are already excluded, but the Sn 1987a limits have always been problematic, and as a general statement, experiments and direct observations should always be performed as a check of astrophysical inferences. There is no concept to feasibly push the sensitivity in $g_{A\gamma\gamma}$ down by more than an order of magnitude across the entire mass range. Pessimistically, an axion of 0.1–10 meV and possessing standard couplings will remain undiscovered, though ideas have been proposed even here (103). Optimistically, a lighter axion ($<$0.1 meV) or one possessing unexpectedly stronger couplings to photons will be discovered, perhaps within a decade. Axionic dark matter could potentially reveal phenomenal detail

about the formation and phase-space structure of our galaxy, as the signal represents the total energy of axion and thus manifest, dramatic Doppler modulation, especially if fine structure exists.

ACKNOWLEDGMENTS

This work was supported under the auspices of the U.S. Department of Energy under Contracts W-7405-Eng-48 at Lawrence Livermore National Laboratory and DE-FG02-97ER41029 at the University of Florida, and by an IBM Einstein Endowed Fellowship at the Institute for Advanced Study. K.Z. was partially supported by the European Union under the ILIAS project, Contract RII3-CT-2004-506222.

The *Annual Review of Nuclear and Particle Science* is online at http://nucl.annualreviews.org

LITERATURE CITED

1. Rogers J. *Limits on the electromagnetic coupling and density of axions*. PhD thesis. Univ. Rochester. 181 pp. (1987)
2. Peccei R, Quinn H. *Phys. Rev. Lett.* 38:1440 (1977); Peccei R, Quinn H. *Phys. Rev. D* 16:1791 (1977)
3. Eidelmann S, et al. (Part. Data Group) *Phys. Lett. B* 592:1 (2004); Backer CA, et al. hep-ex/0602020
4. Weinberg S. *Phys. Rev. Lett.* 40:223 (1978); Wilczek F. *Phys. Rev. Lett.* 40:279 (1978)
5. Preskill J, Wise M, Wilczek F. *Phys. Lett. B* 120:127 (1983); Abbott L, Sikivie P. *Phys. Lett. B* 120:133 (1983); Dine M, Fischler W. *Phys. Lett. B* 120:137 (1983)
6. Sikivie P. *Phys. Rev. Lett.* 51:1415 (1983). Erratum. *Phys. Rev. Lett.* 52:695 (1984); Sikivie P. *Phys. Rev. D* 40:2988 (1985); Krauss L, et al. *Phys. Rev. Lett.* 55:1797 (1985)
7. Kim JE. *Phys. Rep.* 150:1 (1987)
8. Cheng H-Y. *Phys. Rep.* 158:1 (1988)
9. Turner MS. *Phys. Rep.* 197:167 (1990)
10. Raffelt GG. *Phys. Rep.* 198:1 (1990)
11. Raffelt GG. *Stars as Laboratories for Fundamental Physics.* Chicago: Univ. Chicago Press. 664 pp. (1996)
12. Rosenberg LJ, van Bibber KA. *Phys. Rep.* 321:1 (2000)
13. Bradley R, et al. *Rev. Mod. Phys.* 75:777 (2003)
14. Glashow SL. *Nucl. Phys.* 22:579 (1961); Weinberg S. *Phys. Rev. Lett.* 19:1264 (1967); Salam A. *Proc. Nobel Symp., Lerum, Sweden*, pp. 367–77. Stockholm: Almquist-Wiksells (1968)
15. Adler S. *Phys. Rev.* 177:2426 (1969); Bell JS, Jackiw R. Nuov. Cim. A 60:47 (1969)
16. Weinberg S. *Phys. Rev. D* 11:3583 (1975)
17. 't Hooft G. *Phys. Rev. Lett.* 37:8 (1976); 't Hooft G. *Phys. Rev. D* 14:3432 (1976); Jackiw R, Rebbi C. *Phys. Rev. Lett.* 37:172 (1976); Callan CG, Dashen RF, Gross DJ. *Phys. Lett. B* 63:334 (1976)
18. Belavin AA, Polyakov AM, Shvarts AS, Tyupkin YS. *Phys. Lett.* 59B:85 (1975)
19. Pospelov M, Ritz A. *Ann. Phys.* 318:119 (2005)
20. Kobayashi M, Maskawa K. *Progr. Theor. Phys.* 49:652 (1973)
21. Vafa C, Witten E. *Phys. Rev. Lett.* 53:535 (1984)
22. Georgi H, Randall L. *Nucl. Phys. B* 276:241 (1986)
23. Weinberg S. See Ref. 4, p. 224 (1978); Bardeen WA, Tye H. *Phys. Lett. B* 74:229 (1978); Ellis J, Gaillard MK. *Nucl. Phys. B* 150:141 (1979); Donnelly TW, et al.

Phys. Rev. D 18:1607 (1978); Kaplan DB. *Nucl. Phys. B* 260:215 (1985); Srednicki M. *Nucl. Phys. B* 260:689 (1985)
24. Dine M, Fischler W, Srednicki M. *Phys. Lett. B* 104:199 (1981); Zhitnitsky AR. *Sov. J. Nucl. Phys.* 31:260 (1980)
25. Kim J. *Phys. Rev. Lett.* 43:103 (1979); Shifman MA, Vainshtein AI, Zakharov VI. *Nucl. Phys. B* 166:493 (1980)
26. Kim JE. *Phys. Rev. D* 31:1733 (1985)
27. Arkani-Hamed N, Dimopoulos S, Dvali G. *Phys. Lett. B* 429:263 (1998)
28. Arkani-Hamed N, Dimopoulos S, Dvali G. *Phys. Rev. D* 59:086004 (1999)
29. DiLella L, Pilaftsis A, Raffelt GG, Zioutas K. *Phys. Rev. D* 62:125011 (2000)
30. Dienes KR, Dudas E, Gherghetta T. *Phys. Rev. D* 62:105023 (2000)
31. Gross DJ, Pisarski RD, Yaffe LG. *Rev. Mod. Phys.* 53:43 (1981)
32. Davis R. *Phys. Rev. D* 32:3172 (1985)
33. Harari D, Sikivie P. *Phys. Lett. B* 195:361 (1987)
34. Vilenkin A, Everett AE. *Phys. Rev. Lett.* 48:1867 (1982)
35. Sikivie P. *Phys. Rev. Lett.* 48:1156 (1982)
36. Chang S, Hagmann C, Sikivie P. *Phys. Rev. D* 59:023505 (1999)
37. Vilenkin A, Vachaspati T. *Phys. Rev. D* 35:1138 (1987); Davis RL, Shellard EPS. *Nucl. Phys. B* 324:167 (1989); Dabholkar A, Quashnock J. *Nucl. Phys. B* 333:815 (1990)
38. Hagmann C, Sikivie P. *Nucl. Phys. B* 363:247 (1991); Hagmann C, Chang S, Sikivie P. *Phys. Rev. D* 63:125018 (2001)
39. Battye RA, Shellard EPS. *Nucl. Phys. B* 423:260 (1994); Battye RA, Shellard EPS. *Phys. Rev. Lett.* 73:2954 (1994). Erratum. *Phys. Rev. Lett.* 76:2203 (1996)
40. Yamaguchi M, Kawasaki M, Yokoyama J. *Phys. Rev. Lett.* 82:4578 (1999)
41. Lyth D. *Phys. Lett. B* 275:279 (1992)
42. Nagasawa M, Kawasaki M. *Phys. Rev. D* 50:4821 (1994)
43. Vilenkin A. *Phys. Rev. Lett.* 48:59 (1982)
44. Steinhardt PJ, Turner MS. *Phys. Lett. B* 129:51 (1983); Lazarides G, Schaefer R, Seckel D, Shafi Q. *Nucl. Phys. B* 346:193 (1990)
45. Unruh WG, Wald RM. *Phys. Rev. D* 32:831 (1985); Turner MS. *Phys. Rev. D* 32:843 (1985); DeGrand T, Kephart TW, Weiler TJ. *Phys. Rev. D* 33:910 (1986); Hindmarsh M. *Phys. Rev. D* 45:1130 (1992)
46. Linde AD. *JETP Lett.* 40:1333 (1984); Linde AD. *Phys. Lett. B* 158:375 (1985); Seckel D, Turner MS. *Phys. Rev. D* 32:3178 (1985); Lyth DH. *Phys. Lett. B* 236:408 (1990); Linde AD, Lyth DH. *Phys. Lett. B* 246:353 (1990); Turner MS, Wilczek F. *Phys. Rev. Lett.* 66:5 (1991); Linde AD. *Phys. Lett. B* 259:38 (1991)
47. Kaplan DB, Zurek KM. hep-ph/0507236
48. Sikivie P, Ipser JR. *Phys. Lett. B* 291:288 (1992)
49. Sikivie P. *Phys. Lett. B* 432:139 (1998); Sikivie P. *Phys. Rev. D* 60:063501 (1999); Tremaine S. *MNRAS* 307:877 (1999)
50. Sikivie P. *Phys. Lett. B* 567:1 (2003)
51. Hogan CJ, Rees MJ. *Phys. Lett. B* 205:228 (1988); Kolb E, Tkachev II. *Phys. Rev. Lett.* 71:3051 (1993); Kolb E, Tkachev II. *Phys. Rev. D* 49:5040 (1994); Kolb E, Tkachev II. *Ap. J.* 460:L25 (1996)
52. Ansel MA. *Yad. Fiz.* 42:1480 (1985); Ansel MA. *Sov. J. Nucl. Phys.* 42:936 (1985)
53. van Bibber K, et al. *Phys. Rev. Lett.* 59:759 (1987)
54. Ruoso G, et al. *Z. Phys. C* 56:505 (1992)
55. Semertzidis Y, et al. *Phys. Rev. Lett.* 64:2988 (1990); Cameron R, et al. *Phys. Rev. D* 47:3707 (1993)
56. Zavattini E, et al. hep-ex/0512022
57. Zioutas K, et al. (CAST Collab.) *Phys. Rev. Lett.* 94:121301 (2005)
58. Schlattl H, Weiss A, Raffelt GG. *Astropart. Phys.* 10:353 (1999)
59. Hannestad S, Mirizzi A, Raffelt GG. *JCAP* 0507:002 (2005)
60. Bennett CL, et al. *Ap. J. Suppl.* 148:1 (2003)
61. DePanfilis S, et al. *Phys. Rev. Lett.* 59:839 (1987)

62. Wuensch W, et al. *Phys. Rev. D* 40:3153 (1989)
63. Hagmann C, Sikivie P, Sullivan NS, Tanner DB. *Phys. Rev. D* 42:1297 (1990)
64. Moskowitz BE, Rogers J. *Nucl. Instrum. Meth. Phys. Res. A* 264:445 (1988)
65. Hagmann C, et al. *Rev. Sci. Instrum.* 61:1076 (1990)
66. Hagmann C. *A search for cosmic axions.* PhD thesis. Univ. Florida. 126 pp. (1990)
67. Peng H, et al. *Nucl. Instrum. Meth. A* 444:569 (2000)
68. Asztalos SJ, et al. *Phys. Rev. D* 64:092003 (2001)
69. Kinion SD. *First results from a multiple-microwave-cavity search for dark-matter axions*. PhD thesis. Univ. Calif. Davis. 174 pp. (2001)
70. Asztalos SJ, et al. *Phys. Rev. D* 69:011101(R) (2004)
71. Asztalos SJ, et al. *Astrophys. J.* 571:L27 (2002)
72. Duffy L, et al. *Phys. Rev. Lett.* 95(9):091304 (2005)
73. Mück M, et al. *App. Phys. Lett.* 72:2885 (1998)
74. Mück M, et al. *App. Phys. Lett.* 75:3545 (1999)
75. Heitler W. *The Quantum Theory of Radiation*. Oxford, UK: Oxford Univ. Press. 430 pp. 3rd ed. (1954)
76. Kleppner D, Ducas TW. *Bull. Am. Phys. Soc.* 21:600 (1976)
77. Gallagher TF. *Rydberg Atoms*. Cambridge, UK: Cambridge Univ. Press. 509 pp. (1994)
78. Kishimoto Y, et al. *Phys. Lett. A* 303:279 (2002)
79. Tada M, et al. *Phys. Lett. A* 303:285 (2002)
80. Tada M, et al. *Phys. Lett. A* 349:488 (2006)
81. Ringwald A. *Phys. Lett. B* 569:51 (2003)
82. Dicus DA, Kolb EW, Teplitz VL, Wagoner RV. *Phys. Rev. D* 18:1829 (1978)
83. Raffelt GG. *Annu. Rev. Nucl. Part. Sci.* 49:163 (1999)
84. Raffelt GG, Stodolsky L. *Phys. Rev. D* 37:1237 (1988)
85. van Bibber K, McIntyre PM, Morris DE, Raffelt GG. *Phys. Rev. D* 39:2089 (1989)
86. Creswick RJ, et al. *Phys. Lett. B* 427:235 (1998)
87. Lazarus DM, et al. *Phys. Rev. Lett.* 69:2333 (1992)
88. Zioutas K, et al. *Nucl. Instrum. Meth. A* 425:480 (1999)
89. Moriyama S, et al. *Phys. Lett. B* 434:147 (1998)
90. Inoue Y, et al. *Phys. Lett. B* 536:18 (2002)
91. Barth K, et al. *Proc. 2003 Cryog. Eng. Conf. (CEC) Cryog. Mater. Conf. (ICMC), Anchorage, Alaska,* 710:160. AIP Conf. Proc. (2004)
92. Dafni T. *A search for solar axions with the micromegas detector in CAST*. PhD thesis. Technische Universitt-Darmstadt, Germany. 126 pp. (2005); http://astropp.physik.tu-darmstadt.de/publications/publications_de.php
93. Vogel J. *The precision of the tracking system in search of solar axions*, Diploma thesis. Univ. Freiburg, Germany. 134 pp. (2005); http://hpfr02.physik.uni-freiburg.de/arbeiten/diplomarbeiten/vogel.pdf
94. Giomataris Y, Rebourgeard P, Robert JP, Charpak G. *Nucl. Instrum. Meth. A* 376:29 (1996)
95. Struder L, et al. *Astron. Astrophys.* 365:L18 (2001)
96. Altmann J, et al. *Proc. SPIE: X-Ray Opt. Instrum. Mission*, ed. RB Hoover, AB Walker, 3444:350. Bellingham, WA: SPIE (1998); Egle JW, et al. *Proc. SPIE: X-Ray Opt. Instrum. Mission*, ed. RB Hoover, AB Walker, 3444:359. Bellingham, WA: SPIE (1998); Friedrich P, et al. *Proc. SPIE: X-Ray Opt. Instrum. Mission*, ed. RB Hoover, AB Walker, 3444:369. Bellingham, WA: SPIE (1998)
97. Horvat R, Krčmar M, Lakić B. *Phys. Rev. D* 69:125011 (2004)

98. Paschos EA, Zioutas K. *Phys. Lett. B* 323:367 (1994)
99. Avignone FT, et al. *Phys. Rev. Lett.* 81:5068 (1998)
100. Buchmüller W, Hoogeveen F. *Phys. Lett. B* 237:278 (1990)
101. Morales A, et al. *Astropart. Phys.* 16:325 (2002)
102. Bernabei R, et al. *Phys. Lett. B* 515:6 (2001)
103. Sikivie, P, Tanner DB, Wang Y. *Phys. Rev. D* 50:4744 (1994)

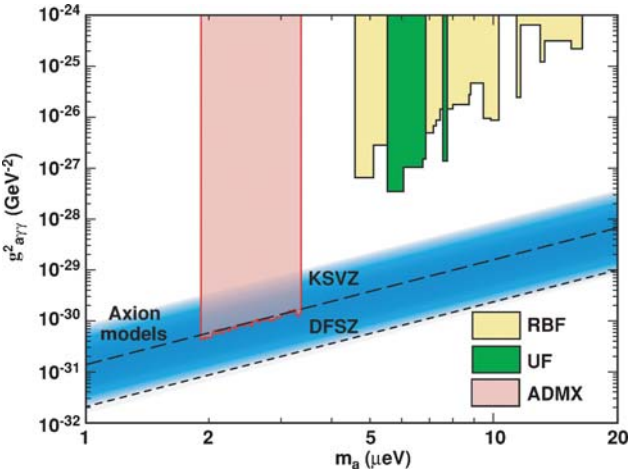

Figure 7 Exclusion regions for the Rochester-Brookhaven-Fermilab (RBF) (61, 62) and University of Florida (UF) (63) experiments. Also shown is the exclusion region for the Axion Dark Matter eXperiment (ADMX) (70). (*Dashed line*) Model of KSVZ (25). (*Dotted line*) Model of DFSZ (24).

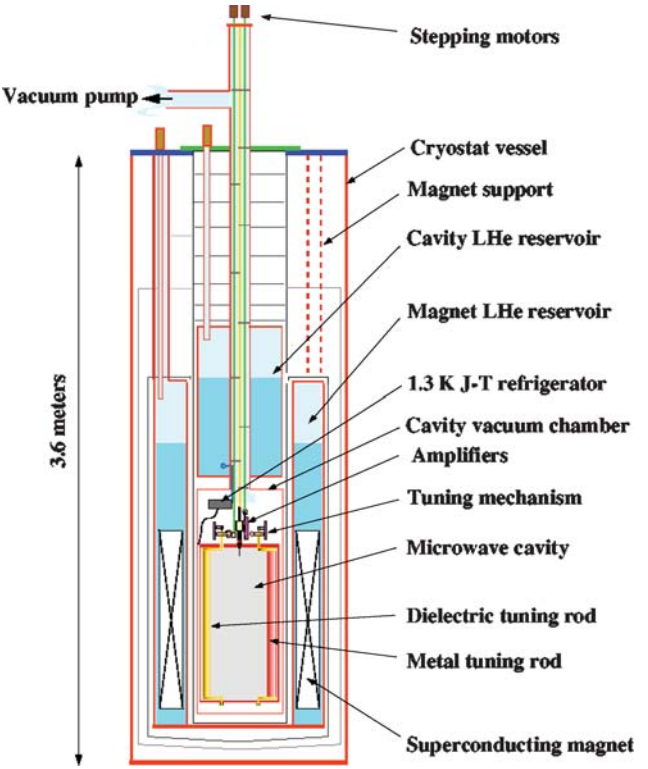

Figure 8 Schematic of the Axion Dark Matter eXperiment (67, 68).

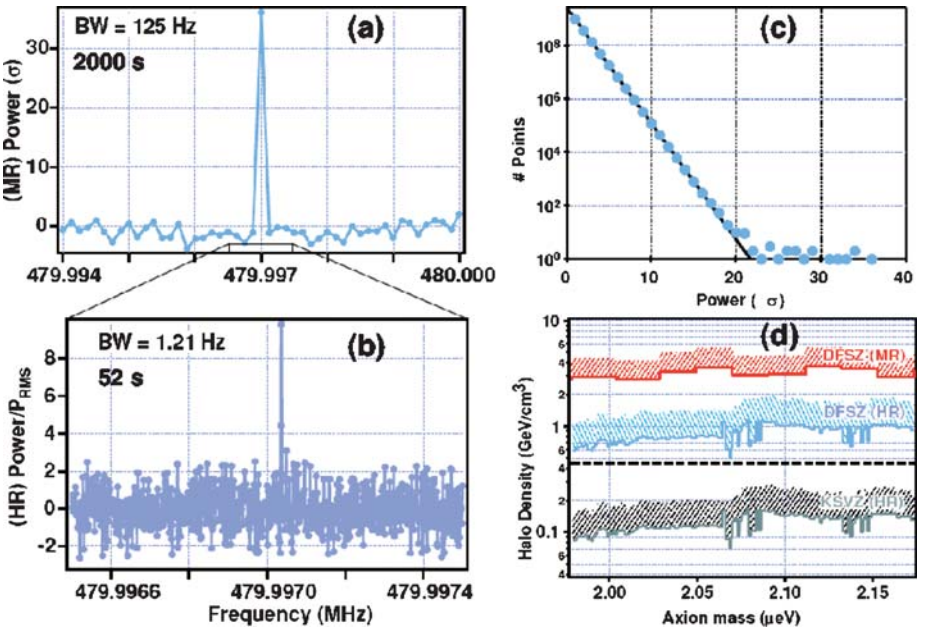

Figure 10 High-resolution analysis by Axion Dark Matter eXperiment. An environmental peak correlated between the (*a*) medium-resolution spectrum and the (*b*) high-resolution spectrum, with identical power. (*c*) The power-fluctuation distribution of the high-resolution Fast Fourier Transform with no co-adding of adjacent bins ($\Delta\nu = 0.019$ Hz). (*d*) Exclusion limits in ρ_A for the high-resolution analysis, assuming a dark matter flow with a narrow velocity dispersion, ≤ 25 m s^{-1} (72).

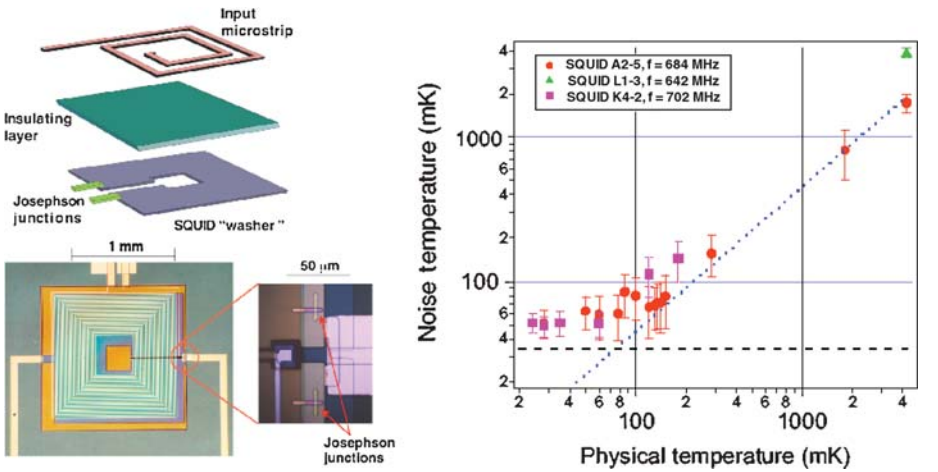

Figure 11 (*a*) Exploded schematic view of a microstrip-coupled SQUID (Super-conducting Quantum Interface Device). (*b*) Noise temperature of a DC SQUID amplifier as a function of physical temperature; note that T_n plateaus at 50 mK, within 50% of the standard quantum limit in the 0.5 GHz range.

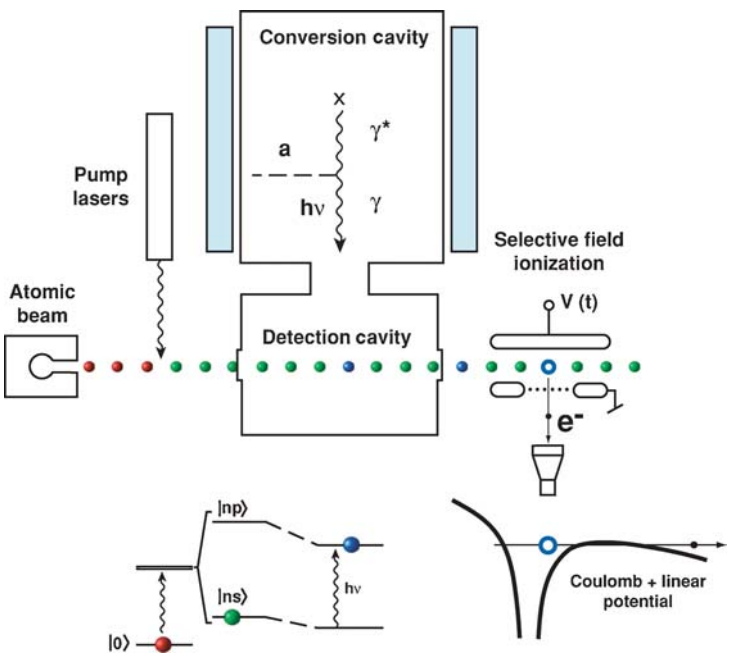

Figure 12 Schematic of the microwave cavity axion experiment with a Rydberg-atom single-quantum detector for detection of the RF photons.

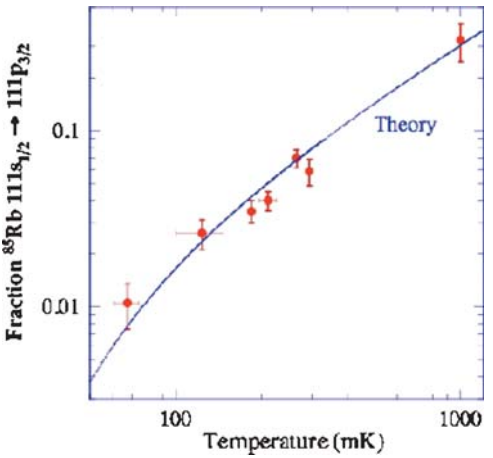

Figure 13 Measurement of blackbody photons in the CARRACK1 (Cosmic Axion Research using Rydberg Atoms in a Resonant Cavity in Kyoto) experiment. The transition to the upper state from the prepared state beamed through the detection cavity $|111s_{1/2}\rangle \rightarrow |111p_{3/2}\rangle$ is compared with absolute (non-normalized) numbers from the theoretical calculation (80).

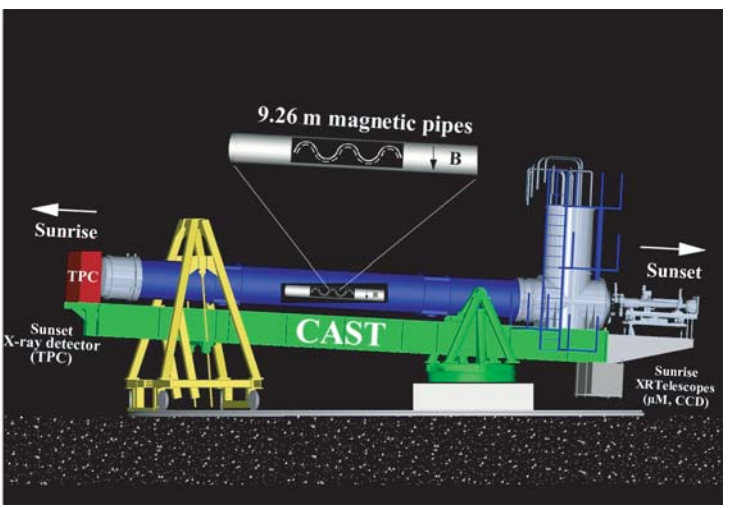

Figure 15 Schematic view of the CERN Axion Telescope (CAST) experimental setup. The 9.26-m-long Large Hadron Collider test magnet is mounted on a platform, allowing a movement of ±8° vertically and ±40° horizontally. The detectors are located at both ends of the magnet, exposed to axion-induced X rays during ∼1.5 h at sunrise and ∼1.5 h at sunset. TPC, time projection chamber; CCD, charge-coupled device. Figure courtesy of Thomas Sahne at CERN.

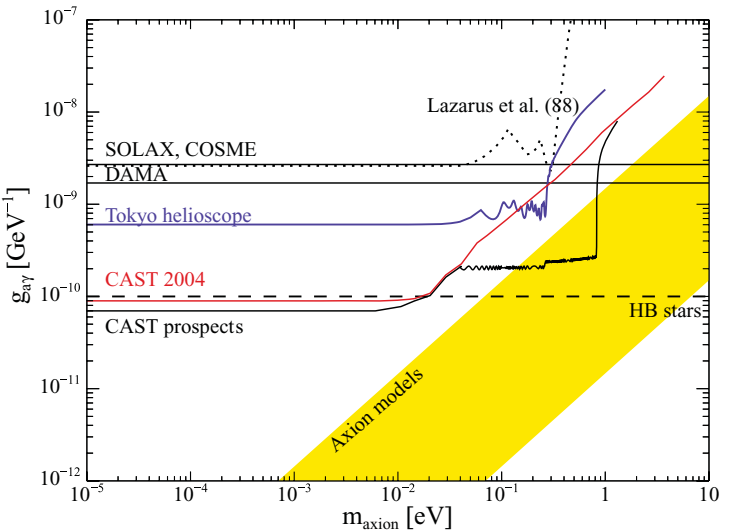

Figure 17 Preliminary results from the CERN Axion Telescope (CAST) data, taken until 2005, compared with other experimental/theoretical results (see also Reference 57). The shaded band represents typical axion models. Also shown is the envisaged future CAST performance (CAST, private communication). HB stars, horizontal-branch stars.

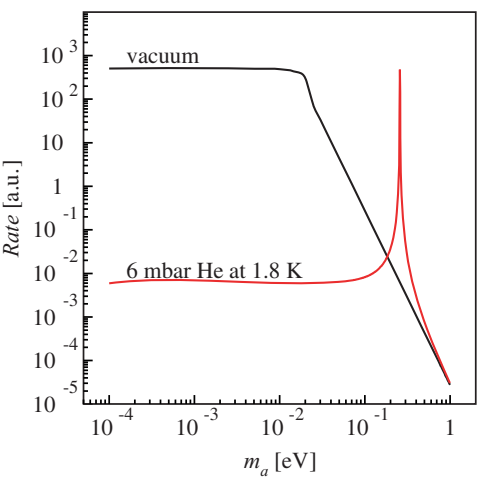

Figure 19 Number of photons that would reach an X-ray detector placed at the end of the magnet versus the rest mass of the incoming solar axion. The upper line stands for the case in which there is vacuum inside the magnet, whereas for the lower line there would be, e.g., helium at 6.0 mbar of pressure.

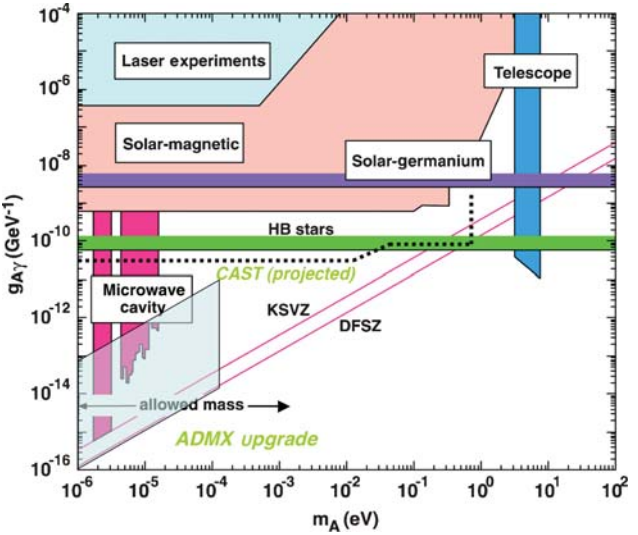

Figure 20 Excluded $g_{a\gamma\gamma}$ versus m_A, with all experimental and observational constraints. ADMX, Axion Dark Matter eXperiment; CAST, CERN Axion Telescope; HB stars, horizontal-branch stars.

Annual Review of Nuclear and Particle Science
Volume 56, 2006

CONTENTS